

Variations in D/H and D/O from new *FUSE* observations¹

Cristina M. Oliveira², H. Warren Moos², Pierre Chayer^{2,3}, and Jeffrey W. Kruk²

ABSTRACT

We use data obtained with the *Far Ultraviolet Spectroscopic Explorer* (*FUSE*) to determine the interstellar abundances of DI, NI, O I, Fe II, and H₂ along the sightlines to WD 1034+001, BD+39 3226, and TD1 32709. Our main focus is on determining the D/H, N/H, O/H, and D/O ratios along these sightlines, with $\log N(\text{H}) > 20.0$, that probe gas well outside of the Local Bubble. *Hubble Space Telescope* (*HST*) and *International Ultraviolet Explorer* (*IUE*) archival data are used to determine the HI column densities along the WD 1034+001 and TD1 32709 sightlines, respectively. For BD+39 3226, a previously published $N(\text{HI})$ is used. We find $(\text{D}/\text{H}) \times 10^5 = 2.14 \pm_{0.45}^{0.53}$, $1.17 \pm_{0.25}^{0.31}$, and $1.86 \pm_{0.43}^{0.53}$, and $(\text{D}/\text{O}) \times 10^2 = 6.31 \pm_{1.38}^{1.79}$, $5.62 \pm_{1.31}^{1.61}$, and $7.59 \pm_{1.76}^{2.17}$, for the WD 1034+001, BD+39 3226, and TD1 32709 sightlines, respectively (all 1σ). The scatter in these three D/H ratios exemplifies the scatter that has been found by other authors for sightlines with column densities in the range $19.2 < \log N(\text{H}) < 20.7$. The D/H ratio toward WD 1034+001 and all the D/O ratios derived here are inconsistent with the Local Bubble value and are some of the highest in the literature. We discuss the implications of our measurements for the determination of the present-epoch abundance of deuterium, and for the different scenarios that try to explain the D/H variations. We present a study of D/H as a function of the average sightline gas density, using the ratios derived in this work as well as ratios from the literature, which suggests that D/H decreases with increasing gas volume density. Similar behaviors by other elements such Fe and Si have been interpreted as the result of depletion into dust grains.

Subject headings: ISM: Abundances — ISM: Evolution — Ultraviolet: ISM — Stars: Individual (WD 1034+001, BD+39 3226, TD1 32709)

¹Based on observations made with the NASA-CNES-CSA *Far Ultraviolet Spectroscopic Explorer*. *FUSE* is operated for NASA by The Johns Hopkins University under NASA contract NAS5-32985.

²Department of Physics and Astronomy, The Johns Hopkins University, 3400 N. Charles St., Baltimore MD 21218

³Primary affiliation: Department of Physics and Astronomy, University of Victoria, P.O. Box 3055, Victoria, BC V8W 3P6, Canada.

1. INTRODUCTION

The present day abundance ratio of deuterium to hydrogen places important constraints on Big Bang nucleosynthesis (BBN) and the chemical evolution of galaxies. Because deuterium is only produced in appreciable amounts in primordial BBN and destroyed in stellar interiors, the measurement of D I/H I in the interstellar medium (ISM) places a lower limit on the primordial abundance of deuterium. In addition, by comparing the ISM abundance of deuterium to its abundance in high-redshift intergalactic gas we should be able to better understand the effects of astration and chemical evolution of galaxies. Measurements of the D/H ratio in intervening clouds of gas seen toward distant quasars have yielded a range of values $D/H = (1.65 - 4.0) \times 10^{-5}$ (O’Meara et al. 2001; Pettini & Bowen 2001; Levshakov et al. 2002, and references therein). Kirkman et al. (2003) measured $D/H = (2.42 \pm_{0.25}^{0.35}) \times 10^{-5}$ toward Q1234+3047 ($z = 2.526$). These authors calculate the value they believe is the best estimate of the primordial D/H abundance, $D/H_{\text{prim}} = (2.78 \pm_{0.38}^{0.44}) \times 10^{-5}$ (1σ errors in the mean), by taking the weighted mean of five D/H measurements toward QSOs ranging from $z = 2.079 - 3.572$. This value is in good agreement with that determined from the cosmic microwave background measurements performed with *WMAP* and previous missions (Spergel et al. 2003). Sembach et al. (2004) found $D/H = (2.2 \pm 0.7) \times 10^{-5}$ for Complex C, a high velocity cloud falling into our galaxy, which has low metallicity and has presumably experienced more stellar processing than the gas seen toward QSOs.

Measurements of D/H in the local ISM have been made with *Copernicus* (e.g. Rogerson & York 1973), *HST*, (e.g. Linsky et al. 1995), *IMAPS*, (Jenkins et al. 1999; Sonneborn et al. 2000), and more recently *FUSE* (e. g. Moos et al. 2002, and references therein). A nearly constant ratio of $D/H = (1.5 \pm 0.1) \times 10^{-5}$ (1σ on the mean) has been obtained in the Local Interstellar Cloud (LIC) by Linsky (1998); recent measurements inside the Local Bubble (LB, $\log N(\text{HI}) \leq 19.2$ Sfeir et al. 1999) appear to be consistent with a single value for D/H in the LB (Moos et al. 2002; Oliveira et al. 2003). From a compilation of measurements from the literature Wood et al. (2004) derive $(D/H)_{\text{LB}} = (1.56 \pm 0.04) \times 10^{-5}$. Using $(D/O)_{\text{LB}} = (3.84 \pm 0.16) \times 10^{-2}$ from Hébrard & Moos (2003) and $(O/H)_{\text{LB}} = (3.45 \pm 0.19) \times 10^{-4}$ from Oliveira et al. (2005) one can derive indirectly $(D/H)_{\text{LB}} = (1.33 \pm 0.09) \times 10^{-5}$. The direct and indirect determinations of $(D/H)_{\text{LB}}$ are only consistent when one considers the 2σ uncertainties in both quantities. A detailed discussion of the possible causes for this discrepancy can be found in Hébrard & Moos (2003).

Outside the Local Bubble, however, there still is not a consistent picture of the D/H behavior. Measurements performed along sightlines probing gas outside the LB suggest variations of the interstellar D/H ratio beyond the Local Bubble, at the distance of a few hundred parsecs. D/H varies for $19.2 \leq \log N(\text{HI}) \leq 20.7$ (e.g. Jenkins et al. 1999; Sonneborn

et al. 2000; Friedman et al. 2002) and apparently remains constant for $\log N(\text{HI}) \geq 20.7$, albeit with a lower value. The possibility of a trend towards low D abundance at high H column densities was noted in the D/O survey by Hébrard & Moos (2003). Wood et al. (2004), using additional measurements and values in the literature, confirmed the trend for D/H. So far, only five measurements for sightlines with $\log N(\text{HI}) \geq 20.7$ have been published. Hoopes et al. (2003), Wood et al. (2004) and Hébrard et al. (2005) measured D/H along five extended lines of sight ($d \geq 500$ pc). The weighted mean of these five measurements yields $\text{D/H} = (0.87 \pm 0.08) \times 10^{-5}$, in clear disagreement with the LB value.

The value of the present-epoch Milky Way abundance of deuterium, $(\text{D/H})_{\text{PE}}$, is still an issue subject to debate. Two opposite explanations have emerged. (Hébrard & Moos 2003) argue for a value of the current-epoch D/H ratio lower than D/H_{LB} , on the basis of the generally low values found for more distant sightlines. On the other hand, Linsky et al. (2005, in prep) argue that an important fraction of deuterium along many sightlines is trapped in a population of grain material and hence the current-epoch deuterium abundance (gas plus grains) is $(\text{D/H})_{\text{PE}} \geq (2.19 \pm 0.27) \times 10^{-5}$. The astration factors, $(\text{D/H})_{\text{prim}}/(\text{D/H})_{\text{PE}}$, derived from both of these scenarios (~ 4 and ~ 1.2 , respectively) challenge current models of galactic chemical evolution.

Because the O/H variations in the diffuse ISM from the LB out to 1 Kpc, are small, consistent with the measurement uncertainties (Meyer et al. 1998; André et al. 2003; Cartledge et al. 2004; Oliveira et al. 2005), OI has been used as a proxy for HI (for a more detailed discussion see Hébrard & Moos 2003, and references therein). Thus D/O and D/H are expected to trace each other in the diffuse ISM. However, how well this works at high column densities is a subject of discussion (Hébrard 2006, and §7.1 of this paper).

At the present time, definitive conclusions are prevented by the limited number of D/H and D/O measurements along high column density sightlines. In this work we present D/H and D/O measurements along three sightlines (WD 1034+001, BD+39 3226, and TD1 32709) with $\log N(\text{HI}) \geq 20.0$. Using data obtained with *FUSE*, *IUE*, and the Goddard High Resolution Spectrograph (GHRS, onboard *HST*) we derive column densities of atomic and molecular species which are then used to determine important ratios (D/H, N/H, O/H, etc.) that can be compared to values in the literature.

This paper is organized as follows. The three targets used for the analyses are described in §2. The observations and data processing are presented in §3. In §4 we determine the column densities of HI, DI, NI, OI, FeII, and H₂ along the WD 1034+001, BD+39 3226, and TD1 32709 sightlines. Lower limits to the column densities of other elements are also reported. The D/H, D/N, D/O, N/H, O/H, and O/N ratios for the three sightlines are presented in §5 and discussed in §6, where evidence for above average D abundance is presented

for the WD 1034+001 and TD1 32709 sightlines. The D/O ratios for the three sightlines are substantially higher than the mean LB value, and thus they considerably increase the scatter in the published D/O ratios. Implications of the derived ratios for hypothetical mechanisms, such as dust depletion and infall of metal poor gas, that try to explain the D/H variations in the Galactic disk are considered in §6.4. Our derived D/H, D/O, and O/H ratios are compared with previously published ratios in §7.1. In §7.2 we consider the relationship between D/O and Fe/O. In §7.3 we perform a study of D/H as a function of the average sightline gas density ($N(\text{H})/d$). Our study indicates that D/H is constant up to densities of 0.10 cm^{-3} and decreases with increasing density after this point, similarly to what has been observed for other elements such as Fe and Si. We summarize our findings in §8. All uncertainties are quoted at the 1σ level unless stated otherwise.

2. THE TARGETS

The properties of the three stars are listed in Table 1. Below we discuss each star in detail.

2.1. WD 1034+001

WD 1034+001 is a hot DO white dwarf with $T_{\text{eff}} = 100,000 \pm \frac{15,000}{10,000} \text{ K}$, $\log g = 7.5 \pm 0.3$, at a distance of $155 \pm \frac{58}{43} \text{ pc}$ (photometric, Werner et al. 1995) in the direction $l = 247.55^\circ$ and $b = +47.75^\circ$. This star was first observed in the ultraviolet with *IUE* by Sion et al. (1985), who identified several photospheric features (C IV, NV, and O V) as well as interstellar features (N I, C II, Si II, Mg II, Si II, and Si III). These authors derived $v_{\text{PH}} - v_{\text{ISM}} \sim 50 \text{ km s}^{-1}$ (v_{PH} and v_{ISM} correspond to stellar and interstellar absorptions, respectively). Non-stellar absorption by C IV was also detected along this sightline by Sion et al. (1985), however the resolution of the data did not allow them to decide whether this absorption had an interstellar or circumstellar origin.

Werner et al. (1995) used GHRS onboard *HST* to observe this target at a resolution of $\sim 20,000$. In addition to stellar absorption by He II, C IV, NV, O V, Si IV, Fe VI, and Fe VII, they also identified absorption by highly ionized species of C IV, NV, and Si IV. With resolution similar to that of Sion et al. (1985), Werner et al. (1995) could not determine whether the absorption had an interstellar or circumstellar origin. Using H I Ly α observations obtained with GHRS in conjunction with NLTE model atmospheres, Werner et al. (1995) determined $\log N(\text{H I}) = 20.05 \pm 0.20$. In this work we reanalyze these H I Ly α observations

together with *FUSE* data to place tighter constraints on $N(\text{HI})$ (see §4.3.1).

Using Sloan Digital Sky Survey data, Hewett et al. (2003) discovered a region of ionized gas around WD 1034+001, seen in $\text{H}\alpha$, $\text{H}\beta$, $[\text{N II}]$, $[\text{O III}]$, and $[\text{S II}]$ emission, with a diameter greater than 2° and identified it with a planetary nebula, Hewett 1. This is one of the largest planetary nebula in the sky, and also the first to be unambiguously associated with a DO white dwarf. Using data obtained with the Southern H-Alpha Sky Survey Atlas, Rauch et al. (2004) found two extended emission structures surrounding WD 1034+001, in addition to the planetary nebula discovered by Hewett et al. (2003). The inner halo has a linear diameter of $16.2 \pm_{4.5}^{6.1} \times 24.3 \pm_{6.8}^{9.1}$ pc while the wider shell has a linear diameter of 27×43 pc (Rauch et al. 2004), at the quoted distance for WD 1034+001 (see Table 1). During its evolution, WD 1034+001 is likely to have passed through a much hotter phase with $T_{\text{eff}} = 150,000\text{K}$, roughly 30,000 years ago (Rauch et al. 2004). These authors estimate that WD 1034+001 is most likely the exciting star of the nebula and the halo given that the recombination time scale in such a low-density ($n_e = 3 \text{ cm}^{-3}$) nebula is longer than 30,000 years.

2.2. BD+39 3226

BD+39 3226, first identified as a sdO by Berger & Fringant (1978), lies at a distance of $290 \pm_{70}^{140}$ pc (*Hipparcos*) in the direction $l = 65.00^\circ$, $b = +28.77^\circ$. Bluhm et al. (1999) determined the abundances of the atomic (HI , DI , etc.) and molecular species (H_2) along the line of sight using data obtained with *IUE* and *ORFEUS II*, and determined $v_{\text{PH}} - v_{\text{ISM}} \sim -255 \text{ km s}^{-1}$. However, the spectral resolution of only $\sim 30 \text{ km s}^{-1}$ for both the *IUE* and *ORFEUS II* datasets led to fairly large uncertainties on the column densities determined with those data. The new *FUSE* data with a resolution of $\sim 20 \text{ km s}^{-1}$ and better S/N ratio allows us to determine more accurate column densities and in addition, offers us the possibility of comparing column densities determined from data obtained with different instruments.

In this work we use the *FUSE* data to revisit the column densities along the BD+39 3226 sightline for the species that have transitions in the *FUSE* bandpass. Since the $\text{Ly}\alpha$ transition of HI is not covered by *FUSE* we use the value reported by Bluhm et al. (1999). These authors used $\text{Ly}\alpha$ observations from *IUE* and *ORFEUS II*, in conjunction with a stellar model with $T_{\text{eff}} = 45,000 \text{ K}$ and $\log g = 5.5$, to determine $\log N(\text{HI}) = 20.08 \pm 0.09$.

2.3. TD1 32709

TD1 32709 (UVO 0904–02) was first identified as a sdO by Berger & Fringant (1980) using data obtained with the Ultraviolet Sky Survey Telescope S 2/68. Using optical data in conjunction with NLTE stellar atmosphere models, Dreizler (1993) determined $T_{\text{eff}} = 46,500 \pm 1,000$ K and $\log g = 5.55 \pm 0.15$. The corresponding photometric distance is $d = 520 \pm 90$ pc ($z = 245 \pm 40$ pc). *IUE* observations covering the Ly α region in combination with *FUSE* data and stellar models allow us to determine $N(\text{H I})$ along this sightline (see §4.3.2). From our work we determine $v_{\text{PH}} - v_{\text{ISM}} = -13$ km s $^{-1}$ (see §4.2.3).

3. OBSERVATIONS AND DATA PROCESSING

3.1. *FUSE* Observations

The *FUSE* observatory consists of four coaligned prime-focus telescopes and Rowland-circle spectrographs that produce spectra over the wavelength range 905 – 1187 Å, with a spectral resolution of $\sim 15 - 20$ km s $^{-1}$ (wavelength dependent) for point sources. Details about the *FUSE* mission, its planning, and on-orbit performance can be found in Moos et al. (2000) and Sahnou et al. (2000).

Table 2 summarizes the *FUSE* observations of the three targets. The data were obtained through the medium size aperture (MDRS, $4'' \times 20''$), in histogram (H) or ttag modes (T). The two-dimensional *FUSE* spectra are reduced using the CalFUSE pipeline v2.4.1 or v2.4.2¹. The processing includes data screening for low quality or unreliable data, thermal drift correction, geometric distortion correction, heliocentric velocity correction, dead time correction, wavelength calibration, detection and removal of event bursts, background subtraction, and astigmatism correction. The spectra are aligned by cross-correlating the individual exposures over a short wavelength range that contains prominent spectral features and then coadded by weighting each exposure by its exposure time, using the CORRCAL software developed by S. Friedman. All the spectra are binned to three pixel samples, or ~ 20 mÅ, for analysis (the line spread function, LSF, is about 11 pixels or ~ 70 mÅ wide). For each target, all the observations were coadded in order to increase the S/N of the dataset. The S/N per unbinned pixel in the SiC 1B channel around 940 Å is 8, 26, and 14, for WD 1034+001, BD+39 3226, and TD1 32709, respectively.

Figures 1, 2, and 3, present the *FUSE* spectra of the three targets. The most prominent

¹The CalFUSE pipeline reference guide is available at http://fuse.pha.jhu.edu/analysis/pipeline_reference.html

interstellar and photospheric lines are labeled; photospheric lines are indicated by [], and H₂ absorption by dashed vertical lines.

4. ANALYSIS

Whenever possible we use apparent optical depth, curve of growth and profile fitting methods (hereafter AOD, COG, and PF, respectively) to determine column densities (see e.g. Oliveira et al. 2003, and references therein for a further discussion of these methods). AOD is used on weak transitions to determine column densities of species that have multiple transitions in the *FUSE* bandpass, which are then compared to the values derived with the other methods. For species that only have saturated transitions in the *FUSE* bandpass we use the AOD technique to place lower limits on the column densities of those species.

We use the COG method to determine the column densities of species that have several transitions in the *FUSE* bandpass (one or more of these transitions must be unsaturated). We measure the equivalent widths of all the non-blended transitions, in all the *FUSE* channels where those transitions are covered, and compare them to check for inconsistencies (due to fixed pattern noise, for instance). A single component Gaussian curve-of-growth is then fit to the measured equivalent widths of the atomic species, allowing us to determine N and b , for each species. For H₂ we fit a single-component Gaussian COG to the equivalent widths of all the J levels, simultaneously. We determine then $N(J)$ and b , common to all J levels.

With PF we fit a single absorption component to one or more non-saturated transitions of the species for which N is being sought. We use the profile fitting code *Owens*, developed by Martin Lemoine and the French *FUSE* Team. Details of how the PF method is used for the analysis of each sightline studied in this paper are given below. More information about the fitting code can be found in Lemoine et al. (2002) and Hébrard et al. (2002).

We follow the procedures outlined in Oliveira et al. (2003) to use these techniques and determine the uncertainties in N associated with each method. We introduce a modification from Oliveira et al. (2003) regarding the PF technique. A single-Gaussian with a FWHM of 10.5 pixels (constant across all wavelengths and channels and during the fitting procedure) is used here to describe the *FUSE* line spread function (LSF), whereas previously the LSF was a free parameter of the fitting procedure during the initial stages of the fit (see Oliveira et al. 2003, for more details). However, since several studies have shown that column densities obtained with fits using variable and fixed LSFs are similar (e.g. Williger et al. 2005) we prefer to decrease the number of degrees of freedom of the profile fitting routine by using a fixed LSF.

All the atomic lines used in the AOD, COG, and PF analyses are shown in Table 3 along with $\log f\lambda$ for each transition. We use the compilation of Morton (2003) for the atomic data and the ones by Abgrall et al. (1993a) and Abgrall et al. (1993b) for the H_2 data. For each star, A, C, and P denote transitions that are used with the apparent optical depth, curve of growth, and profile fitting methods, respectively. Table 4 presents the equivalent widths of the atomic lines used with the COG method for each sightline. After column densities and uncertainties are determined with these different techniques the results are examined to check the consistency between the different methods. The adopted results are a subjective compromise between the values obtained with the several methods used; the uncertainties adopted are such that they in general include the extreme values obtained with the different methods. No attempt was made to combine the different results in any statistical way. The results of the individual methods are also presented (see § 4.2).

In § 4.1 we determine the H_2 column densities along the three lines of sight, atomic column densities are discussed in § 4.2. Determination of the H I column density along the WD 1034+001 and TD1 32709 sightlines is discussed in §4.3.

4.1. Molecular Hydrogen

4.1.1. WD 1034+001

Along this sightline we detect absorption arising from the H_2 rotational levels $J = 0 - 3$. We use AOD, single- b COG and PF to derive the column densities of the $J = 0 - 3$ levels. From the single- b COG fit we derive $b_{\text{COG}} = 3.6 \pm 0.4 \text{ km s}^{-1}$. Profile fitting of the different J levels is done simultaneously with the atomic species along this sightline, under the assumption that the molecular gas does not trace precisely the atomic gas (i.e. atomic and molecular species are fit in different absorption components). Although the velocities of the atomic and molecular component are a free parameter of the fit, no significant velocity differences are found between the two components. The adopted column densities for each J -level are summarized in Table 5. We adopt $\log N(\text{H}_2) = 15.72 \pm 0.13_{0.12}$. The excitation diagram for H_2 along this sightline is presented in the top panel of Figure 4. We derive $T_{02} = 341 \pm 75 \text{ K}$.

4.1.2. BD+39 3226

For this sightline we detect absorption arising from the H_2 rotational levels $J = 0 - 5$. We use AOD, single- b COG and PF to derive the column densities of the $J = 0 - 3$ levels.

The $J = 4, 5$ levels have very low column densities and we use only PF to determine the column densities associated with these two J levels.

From the single- b COG fit to the $J = 0 - 3$ levels we derive $b_{\text{COG}} = 4.3 \pm 0.3 \text{ km s}^{-1}$. Similarly to WD 1034+001, profile fitting of the $J = 0 - 5$ levels is done simultaneously with the atomic species, but in different absorption components. Table 5 presents the adopted column densities for this sightline. We adopt $\log N(\text{H}_2) = 15.65 \pm 0.06$. The excitation diagram for H_2 along this sightline is presented in the middle panel of Figure 4. The populations of the levels with $J \geq 2$ are larger than expected if the different levels were populated according to a Boltzmann distribution with an excitation temperature corresponding to T_{01} (indicated by a dashed line in Figure 4). This nonthermal excitation is the result of pumping by UV photons followed by cascading transitions down through the various rotational levels (Black & Dalgarno 1976). The high J lines can typically be fit by a single excitation temperature. However, in the case of this sightline a single temperature fit to $J = 2 - 5$ clearly overestimates the column densities of the $J = 3$ and $J = 4$ levels. We find that the distribution of H_2 through the different J levels is better described by several temperatures. We derive then $T_{01} = 104 \pm 27 \text{ K}$, $T_{13} = 200 \pm 15 \text{ K}$, and $T_{35} = 953 \pm 158 \text{ K}$.

4.1.3. TD1 32709

We use AOD and PF to determine the column densities of the H_2 rotational levels $J = 0 - 3$. For this sightline, the low column density of each J level implies that the number of absorption lines that could be used with the COG method is small, and hence we do not perform a COG fit for H_2 along this sightline. The consistency of PF results is checked against that of the AOD method. Table 5 presents the adopted $N(J)$ for this sightline. We derive $N(\text{H}_2) = 14.48 \pm 0.12$. The bottom panel of Figure 4 presents the H_2 excitation diagram for this sightline. All the J levels are consistent with a single temperature corresponding to $T_{02} = 292 \pm 83 \text{ K}$.

No HD is detected along any of these sightlines. Typical HD/H_2 ratios along these types of diffuse sightlines are of the order of 1×10^{-5} or less. Considering $N(\text{H}_2)$ quoted in Table 5 we expect $\log N(\text{HD}) < 11$.

4.2. Atomic Species

In this section we discuss the determination of the atomic column densities along the three sightlines. However, determination of $N(\text{HI})$ along the WD 1034+001 and TD1 32709

sightlines will be discussed separately in §4.3. Tables 6, 7, and 8 present the column densities for DI, NI, OI, and FeII obtained with the different methods discussed above. The adopted column densities for the atomic species along the three sightlines are summarized in Table 9.

4.2.1. *WD 1034+001*

We use the AOD method to derive lower limits to the column densities of CII*, CIII, NII, SiII, PII, and ArI, because all the transitions of these species in the *FUSE* bandpass are saturated. The AOD method is also used for weak transitions of DI, NI, OI, and FeII, to determine column densities which are then compared to the column densities determined with the other methods.

We fit a single-Gaussian COG to the measured equivalent widths of DI, NI, OI, and FeII. The four COGs yield b -values in the range $b = 5 - 6 \text{ km s}^{-1}$. Figure 5 presents the curve of growth for OI along this sightline.

With PF we fit a single absorption component to non-saturated lines of DI, NI, OI, and FeII. In order to model the continuum in the vicinity of the DI lines an extra absorption component with HI only, is also included in the fit. This component is not used to derive $N(\text{HI})$ along this sightline. No stellar model is used in the fitting process because the photospheric spectrum is generally flat in the regions of interest. As discussed above, H_2 is also included in the fit, in a different absorption component. The DI lines used in this analysis have a minor blending with H_2 , hence $N(\text{DI})$ is not affected by the assumed $N(\text{H}_2)$.

Along this sightline we also detect absorption by OVI ($\lambda 1032, 1038$), SIII ($\lambda 1012$), and SIV ($\lambda 1063$). OVI absorption has two components, separated by $\sim 50 \text{ km s}^{-1}$. The strongest component falls at the stellar velocity derived by Sion et al. (1985) and is likely of stellar origin. Absorption by SIII, SIV, and the weaker OVI absorption component fall at the velocity of the atomic gas (DI, NI, OI, and FeII) along this sightline. However, we cannot conclude with certainty whether these features have an interstellar or circumstellar origin. Note that as discussed in §2.1, two large ionized halos have been discovered in the vicinity of WD 1034+001. The OVI lines are weak and blended with stellar OVI absorption; we derive $N(\text{OVI})$ with PF, following the method described in §4. The SIII absorption line is strong and likely saturated. We derive only a lower limit to its column density using the AOD technique. The SIV line is blended with an unidentified feature on the blue side, and is likely saturated. We derive a lower limit to its column density using the AOD technique.

Figure 6 presents fits to some of the lines used in the analysis of the WD 1034+001

sightline. The line inside \square is of photospheric origin. Table 6 presents the column densities for DI, NI, OI, and FeII along this sightline, obtained with the three different techniques.

4.2.2. *BD+39 3226*

Bluhm et al. (1999) report the detection of a weak interstellar absorption component at $v_{\odot} = -75 \text{ km s}^{-1}$ (Component B in their Fig. 1), seen in OI ($\lambda 1039$), Si II ($\lambda 1526$), and Fe II ($\lambda 2374$). We see no evidence for such a component in the higher resolution and higher S/N *FUSE* data. Figure 7 displays the absorption profile of Fe II 1144.9 as seen with *FUSE*. This transition is ~ 1.6 times stronger than the Fe II $\lambda 2374$ transition in which Bluhm et al. (1999) claim to see a second component. The *FUSE* data shows only one component at $v_{\odot} = -25 \text{ km s}^{-1}$, consistent with their Component A at $v_{\odot} = -25 \text{ km s}^{-1}$. Close inspection of the OI $\lambda 971.7$ transition (stronger than OI $\lambda 1039$) in our data also shows only one absorption component at the same velocity of Fe II $\lambda 1144.9$. There is however an absorption feature detected in the *FUSE* data, shifted by $\sim -50 \text{ km s}^{-1}$ from OI $\lambda 1039$ (consistent with absorption at $v_{\odot} = -75 \text{ km s}^{-1}$). This feature is due to absorption by stellar N III $\lambda 1038.988$ and $\lambda 1039.0$, at the radial velocity of the star. It is possible that the lower S/N *IUE* data used by Bluhm et al. (1999) have lead them to mistakenly identify coincident noise features with extra absorption components of Fe II and Si II.

Although scattered flux is generally low in the *FUSE* channels (Moos et al. 2000; Sahnou et al. 2000), there is some apparent residual flux, $\leq 4\%$ of the continuum, in the core of the HI Lyman lines (see Fig. 2). Apparent residual flux is also present, albeit at a smaller level, below the Lyman break. This is probably due to the fact that this target was observed in histogram mode. For this type of observation the *FUSE* pipeline takes into account a background model which is scaled only by the exposure time. For instance, WD 1034+001 was observed in time-tag mode. In this case the background model used by the *FUSE* pipeline is scaled to match the observed counts in the unilluminated regions of the detector, hence doing a better job of removing the scattered flux (note how the cores of the HI lines in the spectrum of WD 1034+001 in Fig. 1 have no residual flux). To properly determine column densities it is important to account for this residual flux, which is approximately constant within each channel, but varies between channels. Consequently, we removed this residual flux from all the channels, before performing any analysis of the data (a similar procedure has been used in other D/H analyses, see Hébrard et al. 2002, for an example).

The large separation between stellar and interstellar absorption ($\sim 255 \text{ km s}^{-1}$ Bluhm et al. 1999) along this sightline is high enough to remove the need for using a stellar model to account for the shape of the stellar continuum in the vicinity of the DI lines due to HI

and He II stellar absorption. Hence, no stellar model is used in this analysis.

We use the AOD technique to determine column densities for DI, NI, OI, and FeII, and place lower limits on the column densities of CII, CII*, CIII, SiII, PII, and ArI.

With the COG method we fit single-component Gaussian COGs to the measured equivalent widths of DI, NI, OI, and FeII. No other atomic species detected along this sightline have enough transitions to perform COGs. From the four COGs we derive b -values in the range $b = 5 - 6 \text{ km s}^{-1}$.

With the PF technique we fit a single component to unsaturated lines of DI, NI, OI, and FeII. H₂ is also included in the fit, but in a separate absorption component. The DI lines used in determining $N(\text{DI})$ (see Table 3) with the PF method are not blended with H₂ or stellar absorption (to the best of our knowledge), hence $N(\text{DI})$ is not affected by the H₂ column density.

Weak absorption by O VI $\lambda 1032$ is detected at the same velocity as the one of the low ionization interstellar metals. O VI $\lambda 1038$ is blended with stellar absorption by O VI** and is not used in our analysis. We use AOD and PF to determine $N(\text{O VI})$ along this sightline.

Fits to some of the lines used in the analysis of this sightline are presented in Figure 8. Table 7 presents the column densities for DI, NI, OI, and FeII along this sightline, obtained with the three different techniques.

O I Column Density

To determine $N(\text{OI})$ along the BD+39 3226 sightline we analyze the 919.9 ($\log(f\lambda) = -0.79$), 925.4 ($\log(f\lambda) = -0.49$), and 974 Å ($\log(f\lambda) = -1.82$) OI lines. We derive $\log N(\text{OI}) = 16.33 \pm 0.08$ with the AOD method for the 919.9 Å transition; a similar value is obtained for OI $\lambda 925.4$. We did not use the AOD technique on the weak $\lambda 974$ transition, or measured its equivalent width, because this line is blended on the red side with H₂ ($J = 2$). Figure 9 presents the curve-of-growth for OI along this sightline. From the COG we derive $\log N(\text{OI}) = 16.31 \pm 0.07$, also in good agreement with the AOD-derived $N(\text{OI})$ values from the 919.9 and 925 Å transitions (see Table 7). Figure 10 compares two sets of SiC 1B and SiC 2A data, in the vicinity of the OI $\lambda 974$ transition (data shifted vertically for clarity). Data plotted at the top were calibrated with version 3 of CalFUSE (V3), data at the bottom were calibrated with version 2.4 (V2.4), which was used throughout this work. The discrepancy between V2.4 SiC 1B and SiC 2A data around OI $\lambda 974$ disappears when CalFUSE V3 is used. Hence, for the OI $\lambda 974$ transition, we use the V3 data (no other discrepancies between lines were found when the two datasets were compared). With the PF

technique we determine $N(\text{OI})$ (as described in §4.2.2) by assuming that DI, NI, OI, and Fe II trace the same absorption component. Hence, the b -value of each species is constrained by the b -values of the other species in the absorbing gas. Determining $N(\text{OI})$ with OI $\lambda 974$ only leads to $\log N(\text{OI}) = 16.82 \pm {}^{0.06}_{0.07}$, while a similar fit with only OI $\lambda 919.9$ and $\lambda 925.4$ leads to $\log N(\text{OI}) = 16.51 \pm 0.04$. Fits using either $\lambda 919.9$ or $\lambda 925.4$ alone lead to $N(\text{OI})$ consistent with $N(\text{OI})$ quoted above when these two lines are fit together.

The discrepancy between the $N(\text{OI})$ values derived with or without the $\lambda 974$ OI line (> 0.30 dex in the log) could in principle indicate that there was a problem with saturation with some of the lines used in the analysis. However, the AOD determined $N(\text{OI})$ for $\lambda 919.9$ is in good agreement with the one determined with the same method from the $\lambda 925$ OI line, which is ~ 2 times stronger. This indicates that there is little or no unresolved saturation in these lines, and hence that $N(\text{OI})$ derived from them is reliable. In addition, the COG-derived OI along this sightline (see Figure 9) is in good agreement with the AOD results quoted above.

Overplotting $\log N(\text{OI}) = 16.82$ on the profiles of the $\lambda 919.9$ and $\lambda 925.4$ OI lines clearly indicates that this column density is overestimated, unless one assumes that some unknown effect causes simultaneously the 925.4 \AA and 919.9 \AA lines, in both channels, to be narrower and shallower than they should be. This seems unlikely. Note that the b -values obtained in the fits of the three lines ($\lambda 974$ alone, or $\lambda 919.9$ together with $\lambda 925.4$, or all three transitions simultaneously) is similar.

Three possibilities can be explored to try to explain the disagreement between $N(\text{OI})$ derived from $\lambda 974$ and the one derived from the $\lambda 925$ and $\lambda 919.9$ OI lines: 1) there could be a problem with the f -value of the $\lambda 974$ transition, 2) there could be a problem with the f -values of $\lambda 919.9$ or $\lambda 925$, and 3) there could be a stellar line blended with the $\lambda 974$ OI transition and/or fixed pattern noise in one of the SiC channels (see below). A problem with the f -values of the $\lambda 974$ or $\lambda 919.9$ transitions seems unlikely as Hébrard & Moos (2003) have reported that no inconsistencies were found between $\lambda 974$ and $\lambda 919.9$ in the analysis of the BD+28 4211 sightline. In their OI analysis of the WD 2211–495 sightline Hébrard et al. (2002) performed tests in which $N(\text{OI})$ derived independently from each individual OI transition (including amongst others the $\lambda 919.9$ and $\lambda 925.4$ transitions) was compared to $N(\text{OI})$ derived from fitting all the OI lines simultaneously. They found that $N(\text{OI})$ obtained from fits to the individual lines varied at most by 20% from the value obtained when all the lines were fit simultaneously and concluded that the f -values of the OI transitions used in their study were consistent with each other. The study by Hébrard et al. (2002) indicates then that there are no large discrepancies between the f -values of the $\lambda 919.9$ and $\lambda 925.4$ OI transitions (at most 20%). The discrepancy between $N(\text{OI})$ derived from $\lambda 974$ and the one

derived from the $\lambda 925$ and $\lambda 919.9$ O I lines is much larger than 20%. Figure 10 compares the SiC 1B and SiC 2A data for the BD+39 3226 sightline in the O I $\lambda 974$ region. The positions of two neighboring H_2 lines are also marked. Even though O I is blended on the red side with H_2 ($J = 2$), this blend should have little effect on the determination of $N(\text{OI})$ since the two lines are resolved and $N(H_2)$, $J = 2$, is well constrained by other weak unblended $J = 2$ lines. The most likely possibility is then that part or all of the weak feature falling at the position of O I $\lambda 974$ along the BD+39 3226 sightline is of stellar origin. The spectra of the sdO BD+39 3226 contains many absorption lines, likely of stellar origin, that we are not able to identify, and so it is not surprising that one of them would fall at the expected position of the O I $\lambda 974$ line. We note that because stellar absorption is shifted by $\sim -255 \text{ km s}^{-1}$ from its rest frame wavelength, the possible blend of O I $\lambda 974$ with a stellar line does not affect the $N(\text{OI})$ determination along other sightlines when the $\lambda 974$ transition is used. Finally, there is also the possibility, although unlikely, that $N(\text{OI})$ derived from the $\lambda 974$ transition is correct and some unknown random effect causes $N(\text{OI})$ derived from $\lambda 919.9$ and $\lambda 925.4$ to agree even though these lines might suffer from saturation effects. Taking into account $N(\text{OI})$ obtained with the different methods and disregarding the value derived when the $\lambda 974$ transition is used, we adopt $\log N(\text{OI}) = 16.40 \pm 0.10$.

Hébrard et al. (2005) and Friedman et al. (2005) have cautioned against not using the $\lambda 974$ O I line when deriving $N(\text{OI})$ along high column density sightlines. In particular, Hébrard et al. (2005) has determined a new $N(\text{OI})$ along the Feige 110 sightline using the transition above and found it to be a factor of ~ 2 larger than the original $N(\text{OI})$ reported by Friedman et al. (2002), which did not use the O I $\lambda 974$ line. There are however differences between our work and that of Hébrard et al. (2005) and Friedman et al. (2005) as neither of these authors used the apparent optical method in their analyses and in particular to compare $N(\text{OI})$ derived from the $\lambda 919.9$ and $\lambda 925.4$ lines. As three of the authors of this paper also participated in the original analysis of the Feige 110 sightline by Friedman et al. (2002) we have access to the same dataset used by Hébrard et al. (2005) in the new analysis. Using this dataset we performed AOD measurements of the $\lambda 919.9$, $\lambda 925.4$, and $\lambda 974$ O I lines and found that $N(\text{OI})$ derived from $\lambda 925.4$ ($\log N(\text{OI}) = 16.43 \pm 0.03$) is $\sim 5\sigma$ smaller than $N(\text{OI})$ derived from the $\lambda 919.9$ line ($\log N(\text{OI}) = 16.58 \pm 0.03$). From the $\lambda 974$ line we derive $\log N(\text{OI}) = 16.98 \pm 0.08$ (1σ), in perfect agreement with the new $\log N(\text{OI}) = 17.06 \pm 0.15$ (2σ) quoted by Hébrard et al. (2005). The different results we obtained from the $\lambda 919.9$ and $\lambda 925.4$ lines for the Feige 110 sightline are a strong indication of saturation of one or both of these two lines, and unless one compares the AOD derived $N(\text{OI})$ from $\lambda 919.9$ with $N(\text{OI})$ from a weaker line one can not decide whether $\lambda 919.9$ suffers from saturation or not. As mentioned before, in our case the $N(\text{OI})$ results from $\lambda 919.9$ and $\lambda 925.4$ lines are in excellent agreement, which gives us confidence that our results are not biased due to not

using the $\lambda 974$ transition.

4.2.3. TD1 32709

Along this sightline the separation between stellar and interstellar absorption is ~ 13 km s $^{-1}$. We use the stellar model computed to determine $N(\text{HI})$ (see §4.3 below) to ascertain which ISM lines might suffer from stellar blendings. The stellar model indicates that the profiles of the DI lines used in this analysis (see Table 3) are not affected by the shape of the stellar continuum in the vicinity of these lines, hence no stellar model is needed to determine the column densities discussed below. In addition, the small molecular hydrogen content along this sightline ($\log N(\text{H}_2) = 14.48 \pm {}^{0.12}_{0.11}$, see §4.1.3) implies that the deuterium column density derived below is not sensitive to $N(\text{H}_2)$.

We use the AOD technique on weak lines to determine the column densities of DI, NI, OI, and FeII, which are then compared to N derived with the other methods. CII, CII*, SiII, PII, and ArI only have saturated transitions in the *FUSE* bandpass. We use the AOD method to determine lower limits to their column densities. We use the COG technique to determine the column densities of DI, NI, OI, and FeII. The b -values derived from the four COGs fall in the range 3 – 6 km s $^{-1}$. With PF we fit a single absorption component to unsaturated lines of DI, NI, OI, and FeII. H_2 is also included in the fit, but in a separate absorption component. In order to provide a smooth continuum for the DI lines we also fit HI as an independent component. This fit, however, is not used to determine $N(\text{HI})$. Absorption by OVI ($\lambda 1032, 1037$) is also detected along this sightline but, the small separation between stellar and interstellar absorption along this sightline (~ 13 km s $^{-1}$) does not allow us to determine if this absorption is of stellar or interstellar absorption origin (or both), as stellar and interstellar absorptions are blended.

The curve of growth for OI along this sightline is presented in Figure 11. We derive $\log N(\text{OI}) = 16.45 \pm {}^{0.09}_{0.03}$. Figure 12 presents fits to some of the lines used in the analysis of the TD1 32709 sightline. Table 8 presents the column densities for DI, NI, OI, and FeII along this sightline, obtained with the three different techniques.

4.3. H I Column Densities

4.3.1. WD 1034+001

To determine $N(\text{HI})$ along this sightline we use data obtained by the GHRS onboard *HST*. GHRS observations were obtained in June of 1992, with the G160M grating and the LSA aperture ($R \sim 20,000$) for a total exposure time of 288 s (rootname: z0ye0c08t). Unfortunately these observations cover only the wavelength range 1185 – 1221 Å, which does not include the complete red wing of $\text{Ly}\alpha$. However, the existing data still allow us to determine $N(\text{HI})$.

The calibrated data were retrieved from the Multimission Archive at the Space Telescope Science Institute and no further processing was applied. The error-weighted data, obtained at four different FP-split positions, were combined to increase the signal to noise ratio of the final dataset. We consider the influence on the $\text{Ly}\alpha$ profile of several stellar models with different effective temperatures and gravities. These are described in detail below.

Stellar Model

We computed stellar atmosphere models using the atmospheric parameters determined by Werner et al. (1995), i.e., $T_{\text{eff}} = 100,000 \pm \frac{15,000}{10,000}$ K, $\log g = 7.5 \pm 0.3$, and $\log (\text{He}/\text{H}) = 3.0$. NLTE H+He models were computed with the stellar atmosphere codes TLUSTY and SYNSPEC (see, e.g., Hubeny & Lanz 1995). The line profile of the He II $\lambda 1215$ line uses an approximate Stark broadening treatment developed by Hubeny et al. (1994), while the hydrogen line profile uses the Vidal et al. (1973) theory (Lemke 1997). We define as the best fit model the stellar model with $T_{\text{eff}} = 100,000$ K, $\log g = 7.5$, and $\log (\text{He}/\text{H}) = 3.0$. The 1σ uncertainties in the stellar parameters determined by Werner et al. (1995) are used to compute stellar models that allow us to determine the systematic uncertainties in $N(\text{HI})$ associated with the uncertainties in the stellar models. Determining the H I column density with different stellar models places more credible error bars on $N(\text{HI})$ than using a single stellar model. The statistical uncertainties are derived by using the best fit stellar model. The systematic uncertainties associated with the stellar models are estimated by considering the most extreme stellar models, i.e., those that yield the strongest and weakest stellar $\text{Ly}\alpha$. Figure 13 illustrates such stellar profiles. The figure shows that the best fit stellar model ($T_{\text{eff}} = 100,000$ K, $\log g = 7.5$; solid line) produces a $\text{Ly}\alpha$ line profile that is between the strongest $\text{Ly}\alpha$ line ($T_{\text{eff}} = 90,000$ K, $\log g = 7.8$; dash-dotted line) and the weakest one ($T_{\text{eff}} = 115,000$ K, $\log g = 7.2$).

Ly α Profile Fitting

We use the separation between stellar and interstellar absorptions derived by Sion et al. (1985) and Werner et al. (1995) to align the data and the stellar models. The different models are then scaled by different factors in order to match the spectrum flux over the region 1190 – 1195 Å. The spectrum is then normalized by the different models prior to fitting.

To determine the HI column density we fit three absorption components with independent velocities, one each for HI, DI, and H₂ ($J = 0 - 3$). $N(\text{DI})$ and $N(\text{H}_2)$ are fixed at the adopted values (see Tables 5 and 9) during the fitting procedure. The b -value of the component containing DI is fixed at $b = 5.8 \text{ km s}^{-1}$, derived from the DI COG. In order to constrain b_{HI} we fit also the higher order HI Lyman lines 917 Å, 918 Å, 919 Å, 920 Å, and 926 Å (923 Å is blended with stellar NIV). The Si III line ($\lambda 1206$) is also included in the Ly α fit, in a fourth independent absorption component, so we can use a large continuum region in the blue side of the Ly α wing. The normalized data is fitted in the range 1201.15 – 1221.28 Å; the continuum is fixed at 1.0 during the fitting procedure.

The statistical uncertainties associated with $N(\text{HI})$ are determined by fitting the data normalized by the best fit model, following the procedure outlined in Oliveira et al. (2003). To determine the uncertainties associated with the continuum placement due to the uncertainties in the stellar model we perform two additional fits, in which the continuum level is multiplied by factors of 1.07 and 0.93 during the fitting procedure (corresponding to a 7% change in the continuum level or to a ‘ χ -by-eye’ of 2σ). As mentioned above, the effect of systematic uncertainties associated with the stellar models are determined by using the extreme models discussed above to measure the highest and lowest interstellar $N(\text{HI})$. These models are illustrated in Figure 13. Figure 14 presents the fit to the Ly α region along this sightline, using the best fit stellar model to normalize the data.

We take a conservative approach to combine the different uncertainties by adding them, rather than adding them in quadrature. Taking into account the different uncertainties in the manner discussed above we determine $\log N(\text{HI}) = 20.07 \pm 0.07 (1\sigma)$.

4.3.2. TD1 32709

To determine $N(\text{HI})$ along this sightline we use data obtained with *IUE* and *FUSE*. High dispersion, large aperture *IUE* observations of the Ly α region were obtained in March 1981 (swp13459), March 1994 (swp50226, swp50227), and December 1993 (swp49676, swp49677), for a total exposure time of 53940 s. The calibrated NEWSIPS MXHI data were retrieved

from the Multimission archive at the Space Telescope Science Institute. The data were not processed further.

The different observations of Ly α were coadded (weighted by their uncertainties) to increase the signal-to-noise ratio of the final dataset. A set of stellar models, described below, were computed to take into account the stellar absorption in the vicinity of Ly α . Similarly to WD 1034+001, we consider the influence of several stellar models with different temperatures and gravities, on the Ly α profile.

Stellar Model

We computed NLTE H+He+C+N models using the atmospheric parameters obtained by Dreizler (1993) from fitting the optical spectrum of TD1 32709. These authors determined $T_{\text{eff}} = 46,500 \pm 1,000$ K, $\log g = 5.55 \pm 0.15$, and $\log(\text{He}/\text{H}) = 2$. We define as the best fit model the model corresponding to $T_{\text{eff}} = 46,500$ K, $\log g = 5.55$, and $\log(\text{He}/\text{H}) = 2$, and use the uncertainties in the stellar parameters to compute stellar models which are used to determine the uncertainties in $N(\text{HI})$ associated with the stellar models. We considered also the influence on the adopted He/H by computing another model with $T_{\text{eff}} = 45,000$ K, $\log g = 5.7$ and $\log(\text{He}/\text{H}) = 1$. This produced $N(\text{HI})$ within the uncertainties of the adopted value.

Figure 15 presents the best fit stellar model (solid line), corresponding to $T_{\text{eff}} = 46,500$ K and $\log g = 5.55$, together with the models that produce the strongest ($T_{\text{eff}} = 45,500$ K and $\log g = 5.7$; dashed line) and weakest ($T_{\text{eff}} = 47,500$ K and $\log g = 5.4$; dash-dotted line) stellar absorption. These models are used to determine the systematic uncertainties in $N(\text{HI})$ associated with the stellar models.

Ly α Profile Fitting

We use the stellar CIV doublet at $\lambda 1230$ to align the stellar models with the data. The stellar models are then scaled by different factors to match the spectrum flux in the 1200 Å and 1225 Å regions. Prior to fitting we normalize the data by the different stellar models.

To determine $N(\text{HI})$ we fit three absorption components, one each for HI, DI + OI, and H₂ ($J = 0 - 2$). The column densities of all the species but HI, are fixed at the adopted values (see Tables 9 and 5) during the fitting procedure. The b -value of the component containing DI and OI is fixed at $b = 6.0$ km s⁻¹, derived from the DI and OI COG analyses. Higher order Ly lines (916 – 919 Å) are also included in the fit, to constrain b_{HI} . These Ly lines were chosen because our models indicate that the interstellar absorption spectrum is not

affected by stellar absorption (either from H or He) in this region. Geocoronal emission fills part of the core of the Ly α line and is taken into account during the fitting procedure by introducing a background in the fit. We determine the background level using the blue side of the Ly α core; the airglow emission visible in Figure 15 is not allowed to influence the profile fitting procedure. We estimate the errors associated with this background by performing multiple fits, using the best fit model, where the background is varied between 6 and 12% of the continuum level. Similarly, errors associated with the continuum level are determined by varying the continuum level, using the best fit model. Figure 16 (top panel) presents the fit to the Ly α interstellar absorption when the best fit stellar model is used to normalize the data and with the zero-flux level defined by the blue side of the Ly α wing, yielding $\log N(\text{HI}) = 20.03$. A similar fit, but with the zero-flux level defined by the red side of the Ly α wing is shown in the bottom panel of this figure. This fit yields $\log N(\text{HI}) = 20.12$. The small emission line on the red side of the airglow emission is likely an artifact of the *IUE* data similar to the ones studied by Crenshaw et al. (1996). Taking into account this feature when defining the zero-flux level leads to $N(\text{HI})$ in the range quoted above (20.3–20.12). The statistical uncertainties associated with $N(\text{HI})$ are determined by fitting the data normalized by the best fit model, following the procedure outlined in Oliveira et al. (2003). Taking all these uncertainties into account, by adding them as in the case of WD 1034+001, we determine $\log N(\text{HI}) = 20.03 \pm 0.10$.

5. RESULTS

Table 10 presents several ratios, using the column densities summarized in Table 9. The fraction of H₂ along these sightlines, $f_{\text{H}_2} = 2 \times N(\text{H}_2) / (2 \times N(\text{H}_2) + N(\text{HI}))$, is $\log f_{\text{H}_2} = -4.05 \pm 0.58$, -4.13 ± 0.46 , and -5.25 ± 0.80 for WD 1034+001, BD+39 3226, and TD1 32709, respectively. Hence, for the three sightlines, $N(\text{H}) = N(\text{HI}) + 2 \times N(\text{H}_2) \approx N(\text{HI})$.

5.1. D/H Ratios

We derive $(\text{D}/\text{H}) \times 10^5 = 2.14 \pm_{0.45}^{0.53}$, $1.17 \pm_{0.25}^{0.31}$, and $1.86 \pm_{0.43}^{0.53}$, for WD 1034+001, BD+39 3226, and TD1 32709, respectively. Only the D/H ratio toward TD1 32709 is consistent, at the 1σ level, with the LB value ($\text{D}/\text{H} = (1.56 \pm 0.04) \times 10^{-5}$) derived by Wood et al. (2004). The value of D/H toward WD 1034+001 is one of the highest D/H ratios measured in the nearby interstellar medium. The other high values are $(1.91 \pm_{0.24}^{0.26}) \times 10^{-5}$ (PG 0038+199, Williger et al. 2005), $(2.14 \pm 0.41) \times 10^{-5}$ (Feige 110, Friedman et al. 2002),

$(2.18 \pm 0.22) \times 10^{-5}$ (γ^2 Vel, Sonneborn et al. 2000), $(2.24 \pm 0.64) \times 10^{-5}$ (α Cru, York & Rogerson 1976) and $(2.24 \pm 0.70) \times 10^{-5}$ (LSE 44 Friedman et al. 2005).

The D/H values reported above are averages over the entire sightline; however they are dominated by the gas beyond the Local Bubble. WD 1034+001 is the shortest sightline analyzed in this work, $d = 155 \pm 58_{43}$ pc. Even though the uncertainties on its distance put it close to the Local Bubble boundary (~ 100 pc, Sfeir et al. 1999, however, in some directions the boundary can be at 65 or 250 pc), the bulk of the gas probed by this sightline is outside the Local Bubble ($\log N(\text{H}) < 19.2$). The Local Bubble contribution to the WD 1034+001 D and H column densities can be estimated by assuming $\log N(\text{H}) = 19.2$ and using $\text{D}/\text{H} = 1.56 \times 10^{-5}$ derived by Wood et al. (2004) for the Local Bubble to determine $\log N(\text{D})_{\text{LB}} = 14.39$. Subtracting the LB contribution yields then $\text{D}/\text{H} = 2.23 \times 10^{-5}$ for the gas outside the LB, an insignificant change from the D/H ratio quoted in Table 10 for this sightline and consistent with the quoted uncertainties ($\text{D}/\text{H} \times 10^5 = 2.14 \pm 0.53_{0.45}$). For the BD+39 3226 and TD1 32709 subtracting the LB contribution to the sightline D/H ratios in the manner described above leads to $\text{D}/\text{H} \times 10^5 = 1.12$ and 1.92, respectively, consistent within the uncertainties with the ratios reported in Table 10 for these two sightlines.

5.2. O/H Ratios

We derive $(\text{O}/\text{H}) \times 10^4 = 3.39 \pm 1.06_{0.86}$, $2.09 \pm 0.72_{0.58}$, and $2.45 \pm 0.90_{0.71}$, for WD 1034+001, BD+39 3226, and TD1 32709, respectively. The first and last ratios are consistent, within the quoted uncertainties, with $\text{O}/\text{H} = (3.43 \pm 0.15) \times 10^{-4}$ derived for 13 lines of sight probing gas within 1500 pc (most within 500 pc), with $20.18 \leq \log N(\text{HI}) \leq 21.28$ (Meyer et al. 1998, updated f -value). O/H along the BD+39 3226 sightline is $\approx 1.86\sigma$ away from the Meyer et al. (1998) ratio. Taking into account the Local Bubble contribution to the O/H ratio along the three sightlines using $\log N(\text{H}) = 19.2$ and the O/H ratio derived by Oliveira et al. (2005) for the Local Bubble, $\text{O}/\text{H} \times 10^4 = 3.45 \pm 0.19$, leads to O/H ratios for the gas beyond the LB consistent within the uncertainties with the values quoted in Table 10.

5.3. D/O Ratios

We derive $(\text{D}/\text{O}) \times 10^2 = 6.31 \pm 1.79_{1.38}$, $5.62 \pm 1.61_{1.31}$, and $7.59 \pm 2.17_{1.76}$, for WD 1034+001, BD+39 3226, and TD1 32709, respectively. Hébrard & Moos (2003) derived $\text{D}/\text{O} = (3.84 \pm 0.16) \times 10^{-2}$ for the Local Bubble from measurements along 14 sightlines. All the D/O ratios reported here are inconsistent, at the 1σ level, with the Local Bubble value, and are some

of the highest D/O ratios measured in the ISM. The implications of this will be discussed below.

5.4. N/H, O/N, and D/N Ratios

The N/H ratios computed for the three sightlines, $(\text{N}/\text{H}) \times 10^5 = 7.76 \pm \frac{2.82}{2.20}$, $5.89 \pm \frac{2.04}{1.63}$, and $8.91 \pm \frac{3.26}{2.59}$ (for WD 1034+001, BD+39 3226, and TD1 32709, respectively), are all consistent, within the uncertainties, with $\text{N}/\text{H} = (7.5 \pm 0.4) \times 10^{-5}$ derived by Meyer et al. (1997).

We derive $\text{O}/\text{N} = 4.37 \pm \frac{1.79}{1.38}$, $3.55 \pm \frac{1.30}{1.03}$, and $2.75 \pm \frac{1.01}{0.80}$. These are consistent, at the 1σ level (1.34σ for TD1 32709), with $\text{O}/\text{N} = 4.1 \pm 0.3$ derived using the values of O/H and N/H determined by Meyer et al. (1998) and Meyer et al. (1997).

The D/N ratios for the three sightlines are $(2.75 \pm \frac{1.00}{0.78}) \times 10^{-1}$, $(2.00 \pm \frac{0.57}{0.46}) \times 10^{-1}$, and $(2.09 \pm \frac{0.60}{0.49}) \times 10^{-1}$ (for WD 1034+001, BD+39 3226, and TD1 32709, respectively).

5.5. N from *FUSE* vs. N from *ORFEUS* for the BD+39 3226 sightline

Table 11 displays, side by side, the column densities of several species derived in this work from *FUSE* data and the column densities derived by Bluhm et al. (1999) using *ORFEUS* and *IUE* data. The column densities for DI, OI, FeII, and H_2 ($J = 0, 1, 3$) are consistent within the quoted uncertainties. For these species, using the *FUSE* data to determine their column densities leads in all cases to a significant improvement of the uncertainties. This is particularly important for DI, NI, and OI, for which we want to determine ratios relative to HI as accurate as possible. The value of $N(\text{NI})$ determined by Bluhm et al. (1999) is substantially smaller than the one determined in this work; $\log N(\text{NI}) = 14.75 \pm 0.25$ vs. 15.85 ± 0.10 . We suspect this is because the weakest NI line used by Bluhm et al. (1999) to determine $N(\text{NI})$ ($\lambda 964.6256$) suffers from considerable saturation, leading to an underestimation of the value $N(\text{NI})$.

6. DISCUSSION

6.1. WD 1034+001

The WD 1034+001 sightline has one of the highest D/H ratios reported in the literature, $D/H = (2.14 \pm {}^{0.53}_{0.45}) \times 10^{-5}$, 1.29σ above D/H_{LB} derived by Wood et al. (2004). However, its O/H and N/H ratios are consistent at the 1σ level with previous measurements (Meyer et al. 1998, 1997). A D/H ratio consistent with the LB value ($\sim 1.56 \times 10^{-5}$), would require $\log N(HI) = 20.21$. In such case, the O/H and N/H ratios ($2.47 \pm {}^{0.80}_{0.63} \times 10^{-4}$ and $(5.66 \pm {}^{2.06}_{1.60}) \times 10^{-5}$, respectively) would still be consistent with the values derived by Meyer et al. (1998) and Meyer et al. (1997), while not affecting the high D/O ratio (the same percentage uncertainties were used for the required $N(HI)$ as the ones derived in this work). In this scenario $\sim 34\%$ of the HI would have been missed in our analysis. It seems unlikely that $N(HI)$ along this sightline could be underestimated by such a large factor. On the other hand, a value of $\log N(DI) = 15.26$ (38% smaller than our derived value) together with our derived $N(HI)$ would also lead to D/H consistent with the LB value, without affecting the O/H and N/H ratios. In this scenario, using the same uncertainties for the required $N(DI)$ as the ones derived in this work, we would find $D/O = (4.57 \pm {}^{1.43}_{1.16}) \times 10^{-2}$. This is lower than our derived value of $(6.31 \pm {}^{1.79}_{1.38}) \times 10^{-2}$, and consistent with the Local Bubble value derived by Hébrard & Moos (2003). We derived $N(DI)$ along this sightline using three different methods, AOD, COG, and PF (see Table 3), and it is unlikely that $N(DI)$ has been overestimated.

Linsky et al. (2005, in prep) looked at correlations between the D/H ratio and other parameters, such as the depletions of Fe and Si, and the kinetic temperature of H_2 (T_{01}), in order to try to understand what is the total deuterium abundance in the local Galactic disk. They found that sightlines with higher Fe and Si depletions correspond in general to lower D/H ratios and that sightlines with high T_{01} have typically higher D/H ratios.

The Fe/H ratio for this sightline, $Fe/H = (1.07 \pm {}^{0.33}_{0.27}) \times 10^{-6}$ (corresponding to $\log(FeII/HI) = -5.97$), is lower than would be expected for this D/H ratio according to Figure 3 of Linsky et al. (2005, in prep). Using the solar abundance of Fe from Asplund et al. (2004), $[Fe/H]_{\odot} = -4.55$, the depletion of Fe along this sightline is $D(Fe) = -1.42$. This is an unusual sightline, for which non-stellar absorption by CIV, NV, OVI, SiIV, SIII, and SIV, has been detected (Sion et al. 1985; Werner et al. 1995, and this work), in addition to the large elliptic halos seen in emission (see §2.1).

The presence of highly ionized species, the high D/H and lower than expected Fe/H, and the typical O/H and N/H ratios are consistent with a scenario in which D is released from the grains, but not much Fe. Perhaps the high radiation field of WD 1034+001 plays

a special role for this sightline. A similar mechanism has been proposed by Linsky et al. (2005, in prep) to explain the high D/H and low Fe/H ratios along the sightline to γ^2 Vel.

6.2. BD+39 3226

For the BD+39 3226 sightline the D/H ratio is only slightly inconsistent with the LB value (1.15σ below). For this sightline, D/H and Fe/H ($(1.17 \pm 0.34) \times 10^{-6}$) follows the correlation derived by Linsky et al. (2005, in prep) for these quantities. Even though interstellar O VI is detected along this sightline, we found no evidence of other highly ionized species (such as C IV, N V, Si IV, S III, or S IV) in either the *FUSE* or *IUE* data for this star. In this case the separation between stellar and interstellar absorption is high enough (~ 255 km s $^{-1}$) to allow for a definitive detection, should an interstellar feature be present. It is possible that along this sightline O VI is formed in evaporative interfaces between cool clouds and the hot and diffuse gas in the Local Bubble. This mechanism has been invoked by Oegerle et al. (2005) to explain the presence of O VI along the sightlines to several white dwarfs inside the Local Bubble. D/O along this sightline, $(5.62 \pm 1.61) \times 10^{-2}$, is not consistent at the 1σ level with the D/O ratio derived for the LB by Hébrard & Moos (2003), $D/O = (3.84 \pm 0.16) \times 10^{-2}$. This is however, in part due to the low O/H ratio derived here for this sightline, $O/H = (2.09 \pm 0.72) \times 10^{-4}$, which is 1.86σ below the O/H ratio derived by Meyer et al. (1998). This O/H ratio is lower than what has been derived in similar studies (see §7.1) and might be indicative of variations of the O/H ratio. Using the O/H ratio derived by the authors above yields $D/O \sim 3.4 \times 10^{-2}$, in closer agreement with the D/O LB value reported above.

6.3. TD1 32709

The TD1 32709 sightline presents a D/H ratio consistent at the 1σ level with the LB, while D/O is inconsistent within the quoted uncertainties at the 2σ level. O/H is lower than the value derived by Meyer et al. (1998) by 1.09σ . If we assume that the D/H and D/O ratios are high due to $N(\text{DI})$ being overestimated then we would need $\log N(\text{DI}) = 15.22$ to bring D/H closer to the LB value. Using the same uncertainties for the required DI as the ones derived in this work (0.05 dex), the D/O ratio would still be high at $(6.31 \pm 1.80) \times 10^{-2}$, even with this reduced value for $N(\text{DI})$. It is unlikely that $N(\text{HI})$ has been over or underestimated, as a lower $N(\text{HI})$ would lead to an even larger D/H ratio, while a larger $N(\text{HI})$ would lead to an even smaller O/H ratio. Increasing $N(\text{OI})$ so that O/H agrees with the Meyer et al. (1998) value still leads to a high D/O ratio, $(5.43 \pm 1.55) \times 10^{-2}$.

(assuming that the increased $N(\text{OI})$ has the same uncertainties as the one derived in this work). The only possibility to reconcile the D/H and D/O ratios along this sightline with the LB values would be for D and O to be simultaneously over and underestimated by 1.6σ and 1.5σ , respectively. However this is unlikely given the number of transitions and methods used to determine $N(\text{DI})$ and $N(\text{OI})$.

For this sightline the Fe/H ratio ($(0.83 \pm_{0.24}^{0.30}) \times 10^{-6}$) is lower than would be expected for the D/H ratio according to Figure 3 of Linsky et al. (2005, in prep). We searched the *IUE* data for this star for absorption by highly ionized species such as C IV, N V, and Si IV. However because the separation between stellar and interstellar absorption is low ($\sim 13 \text{ km s}^{-1}$) we cannot determine if the detected absorptions are of stellar or interstellar origin (or both), similarly to what we had concluded for the O VI absorption detected in the *FUSE* data (see §4.2.3).

6.4. Implications for models that explain D/H variations

The high D/H ratios derived for the WD 1034+001 and TD1 32709 sightlines increase the sample of sightlines for which a high D/H ratio has been found. These measurements strengthen the argument that these high ratios can not be due to some systematic problem associated with the different analyses (see also discussion below) or that they are peculiar cases. In particular, it has been argued that the high D/H ratios found in the ISM could be due to systematic effects that affect the $N(\text{HI})$ measurements (Hébrard et al. 2005). Because the D/O ratios derived for these two sightlines are also high and independent of $N(\text{HI})$, the high D/H ratios are likely due to a high abundance of D and not to a systematic problem with the $N(\text{HI})$ determination (see also discussion in §7.1). In addition, the high D/O ratios, together with O/H ratios consistent with the Meyer et al. (1998) results, contradict the argument by Hébrard (2006) against a high present-epoch D/H ratio, on the basis that no correspondingly high D/O ratios have been measured. It is also hard to explain these high D/H ratios on the basis of localized infall of metal poor gas, as one would expect the O/H and N/H ratios for these sightlines to be affected as well. In addition, several studies of the O/H ratio (Meyer et al. 1998; André et al. 2003; Cartledge et al. 2004; Oliveira et al. 2005) have shown that this ratio is constant across a large range of $N(\text{OI})$, distance to targets, and average sightline gas density. However, note that in a special case where the infalling gas had a high D/H ratio and metallicity comparable to the local ISM value of Meyer et al. (1998), such a mechanism could not be ruled out. Variable astration in which the amount of D burned in the interior of stars and O produced, varies from sightline to sightline, seems also to be an unlikely mechanism for explaining the high D/H ratios. In the case of WD 1034+001 and

TD1 32709 less deuterium would have to have been destroyed by astration and consequently less O would have been produced by supernovae. This scenario seems implausible because it implies that astration rates would have to be variable on short distance scales in order to explain the nearby sightlines with LB-like D/H ratios and also because it is not supported by our derived O/H and N/H ratios. In addition, in both the infall and variable astration scenarios, these processes would have to occur in a time smaller than the typical mixing time-scale of 350 Myr (de Avillez & Mac Low 2002). Our results support the idea that some sightlines in the Milky Way ISM have high D/H ratios. Linsky et al. (2005, in prep) have used the existence of these sightlines together with the deuterium dust-depletion model of Draine (2004) to argue for a high present-epoch abundance of deuterium. Linsky et al. (2005, in prep) estimate the total abundance of D (in gas + dust) in the local disk of the Galaxy, $D/H \geq (2.19 \pm 0.27) \times 10^{-5}$, by taking the weighted average of the ratios for the five sightlines with the highest values. Our new measurements for WD 1034+001 and TD1 32709 are in good agreement with this estimate. Below we compare our new measurements with ratios from the literature.

7. COMPARISON WITH PREVIOUS MEASUREMENTS

7.1. D/H, O/H, and D/O vs. $N(H)$

Figure 17 presents D/H, O/H and D/O ratios (1σ uncertainties, top, middle, and bottom panels, respectively) as a function of the total hydrogen column density, $N(H)$, along the sightline. The data used in this figure are presented in Table 12. Sightlines for which all the ratios are available are marked by asterisks (literature values) and filled circles (this work). The data in this plot uses the ratios derived in this work together with the compilation by Wood et al. (2004) and the values of Friedman et al. (2005) and Hébrard et al. (2005). Sightlines for which no $N(O)$ is available are marked with open squares in the top panel (uncertainties displayed as dotted lines for clarity of the plot). Sightlines displayed by open squares with dashed error bars in the bottom panel (corresponding to D/O) do not have $N(H)$ measurements available. For these sightlines we estimate $N(H)$ using $N(O I)$ and the O/H ratio of 3.43×10^{-4} derived by Meyer et al. (1998). Also plotted are the Local Bubble values of $D/H = (1.56 \pm 0.04) \times 10^{-5}$ (top panel, Wood et al. 2004) and $D/O = (3.84 \pm 0.16) \times 10^{-2}$ (bottom panel, Hébrard & Moos 2003). Dashed vertical lines mark the approximate position of the Local Bubble ($\log N(H) < 19.2$), and $\log N(H) = 20.7$, where a new low and relatively constant D/H ratio seems to emerge. The value of $O/H = (3.43 \pm 0.15) \times 10^{-4}$ derived by Meyer et al. (1998) for the local ISM is also marked (solid and dashed lines in the middle panel of Figure 17).

For the range of hydrogen column densities $19.2 < \log N(\text{H}) < 20.7$, assuming a constant D/H ratio yields the weighted mean $(\text{D}/\text{H}) \times 10^5 = 1.18 \pm 0.05$ (1σ on the mean) and $\chi_\nu^2 = 5.9$ for 16 degrees of freedom (where χ_ν^2 is the total χ^2 divided by the number of degrees of freedom, ν). Because some of the ratios in Table 12 have asymmetric uncertainties we use the average of the uncertainties on each ratio to compute the weighted mean and the uncertainty in the weighted mean for D/H and for the other ratios discussed below. One can consider two possibilities to explain the high value of χ_ν^2 . The scatter is real and variations of the D/H ratio do exist, or the uncertainties of the individual measurements have been underestimated. This last possibility can be explored by assuming that the scatter in D/H for $19.2 < \log N(\text{H}) < 20.7$ is due to some random systematic error in the determination of D/H, unaccounted for in the quoted uncertainties. One can then estimate by how much the uncertainties would have to be increased to obtain $\chi_\nu^2 = 1$. Assuming further that this error can be expressed as a fraction of D/H, and that it is added in quadrature to the quoted uncertainty $\sigma_{\text{D/H}}$, $\sigma_{\text{new}} = (\sigma_{\text{D/H}}^2 + f^2 \times (\text{D}/\text{H})^2)^{0.5}$, we derive $f = 0.40$. This implies that the unknown systematic errors would have to be 40% of D/H. Such a high uncertainty seems unlikely. If we also add the ratios for $\log N(\text{H}) > 20.7$ to the dataset, we derive the weighted mean $\text{D}/\text{H} = (1.10 \pm 0.04) \times 10^{-5}$ with $\chi_\nu^2 = 5.1$ for 21 degrees of freedom, and calculate $f = 0.34$, still a high and unlikely value. These results show that it is unlikely that the scatter in D/H is due to unknown systematic uncertainties associated with the different measurements, and that it is real.

As mentioned above, the apparent lack of scatter in the D/O ratios, has been used as an argument against the existence of sightlines with high D/H ratios (Hébrard et al. 2005). One has however to be careful in analyzing these ratios, as they depend on both the $N(\text{D})$ and $N(\text{O})$ values. For instance, there are different ways of producing a low D/O. One can have a low D/H ratio, and normal O/H, or a normal D/H and a high O/H (where normal refers to the LB value for D/H and to the Meyer et al. 1998, value for O/H). This last way must not be common as several studies have concluded that O/H is constant throughout a large range of $N(\text{H})$ (see for example André et al. 2003; Cartledge et al. 2004, and Oliveira et. al. 2005). However, as shown in Figure 17, four out of the five sightlines with $\log N(\text{H}) > 20.7$, also have O/H ratios inconsistent with the Meyer et al. (1998) value (solid and dashed horizontal lines in the middle plot). For the mean of these five points we find $\text{O}/\text{H} = (5.33 \pm 0.36) \times 10^{-4}$. However $\chi_\nu^2 = 5.3$ for four degrees of freedom, indicating that a single mean may not be appropriate. In other words, for four of these targets D/O is lower than it would have been, if these sightlines had normal O/H ratios. Because of the high average O/H value and considering that the number of measurements at large $N(\text{H})$ (> 20.7 in the log) is statistically small, we think it is necessary when estimating the deuterium abundance at high column densities (which according to the suggestion of Hébrard & Moos 2003, may be

the present epoch Milky Way abundance) to consider both D/H and D/O measurements. In addition, the use of the Meyer et al. (1998) value for O/H to convert the average D/O in this region to the average D/H yields an estimate that is low when compared to the direct D/H measurements in this $N(\text{H})$ region, not unlike what happens when we do the same exercise for the Local Bubble.

The five points with high H column density presented in Figure 17 are near the limit of deuterium column densities that can be measured with an instrument with *FUSE*-like properties. The deuterium lines used in these analysis (Hoopes et al. 2003; Wood et al. 2004; Hébrard et al. 2005) would have been saturated if the D/H ratios along these sightlines were similar or larger than the LB D/H value ($\sim 1.56 \times 10^{-5}$). Hence, there is a bias against measuring high D/H ratios at these large H column densities. This could explain in part why only a few high D/H ratios have been reported in the literature.

Additionally, to try to understand the behavior of the D/O ratio in the regime $19.2 < \log N(\text{H}) < 20.7$ and the apparent lack of scatter in D/O compared to D/H, we can consider the O/H ratios for the sightlines for which $\text{D}/\text{H} > 1.9 \times 10^{-5}$ in the top panel of Figure 17 (α Cru, γ^2 Vel, WD 1034+001, Feige 110, PG 0038+199 and LSE 44; as a function of increasing $N(\text{H})$). For these sightlines with high D/H, one would expect also a high D/O, assuming that O/H is similar to the Meyer et al. (1998) value, hence producing more scatter in the D/O measurements. However, two of these sightlines do not have O/H measurements (α Cru and γ^2 Vel), while Feige 110, PG 0038+199, and LSE 44 have abnormally high O/H ratios (see Table 12). The remaining sightline (WD 1034+001) has O/H consistent with the Meyer et al. (1998) value. Hence, the apparent lack of scatter in the D/O ratio, which has been used as an argument against a high present-epoch D/H ratio, is the result of small number statistics, and cannot be used to draw definitive conclusions about the behavior of the D/O ratio in this regime of $N(\text{H})$.

7.2. D/O vs. Fe/O

Linsky et al. (2005, in prep) have looked at the correlation between the deuterium abundance and the depletion of Fe and found that in sightlines with low D/H ratios Fe is typically more depleted than in sightlines with higher D/H ratios. A different way of considering the relationship between the deuterium and iron abundances is to look at D/O versus Fe/O. By taking the ratio of these abundances relatively to oxygen rather than to hydrogen one can avoid systematic problems that might affect the determination of $N(\text{HI})$ (as could be the case for the Feige 110 sightline, as argued by Hébrard et al. 2005). Figure 18 presents D/O as a function of Fe/O. The solid line represents the fit to all data points

in this plot, yielding $D/O = (2.04 \pm 0.15) \times 10^{-2} + (1.56 \pm 0.30) \times 10^{-2} \times Fe/O$, with $\chi^2 = 76$ for 18 degrees of freedom (only uncertainties in D/O taken into account). This fit is mostly influenced by the sightline with the largest Fe/O ratio and small D/O uncertainties, G191–B2B, represented by a square in the plot. Removing this sightline from the fit yields $D/O = (0.99 \pm 0.23) \times 10^{-2} + (5.64 \pm 0.73) \times 10^{-2} \times D/O$, with $\chi^2 = 39$ for 17 degrees of freedom. The other three sightlines represented by squares also have Fe/O ratios which are inconsistent with the trend displayed by the majority of the data plotted in Figure 18. Excluding all the sightlines displayed by squares in the plot from our fit increases the slope slightly more yielding $D/O = (0.47 \pm 0.28) \times 10^{-2} + (7.85 \pm 0.99) \times 10^{-2} \times Fe/O$, with $\chi^2 = 16$ for 14 degrees of freedom. The probability of χ^2 being larger than 16 for 14 degrees of freedom is $\sim 30\%$. Thus, the trend of decreasing Fe/H with decreasing D/H observed by Linsky et al. (2005, in prep) is also observed when one considers D/O versus Fe/O . We note however that there is no particular reason for not taking into account the points displayed in Figure 18 by squares or that it is theoretically expected that $N(D)$ depends linearly on $N(Fe)$.

7.3. D/H and $\langle n_H \rangle$

Another way of trying to understand the behavior of D/H in the ISM, besides looking for correlations with the abundances of other species (e.g., Prochaska et al. 2005, Linsky et al. 2005, in prep), is to study D/H as a function of the average sightline gas volume density, $\langle n_H \rangle = N(H)/d$.

Elemental abundances measured in the interstellar gas in the solar vicinity are generally depleted with respect to the solar values (Morton 1974; Jenkins et al. 1986). This depletion effect has been commonly interpreted as the result of a fraction of the elements being locked up in dust grains (Jenkins 2004). Furthermore, several studies have shown that the strength of the depletions increases as the average gas density increases (see e. g., Savage & Bohlin 1979; Harris et al. 1984; Spitzer 1985; Jenkins et al. 1986; Jenkins 1987; Crinklaw et al. 1994). The idea that D might be depleted in grains was first proposed by Jura (1982) and updated recently by Draine (2004) (see also Draine 2003). Harris et al. (1984) looked for a correlation between the deuterium abundance and the sightline density. Using *Copernicus* data for 14 sightlines and a limited range of densities, they found no evidence of significant depletion of interstellar deuterium. However, since *Copernicus*, several space-born observatories (*IMAPS*, *HST*, *FUSE*) have been used to measure the interstellar abundance of deuterium and there are now D/H measurements for more than forty sightlines. It is then appropriate to revisit the relationship between D/H and the average sightline gas density.

We use the simple model developed by Spitzer (1985) (see also Jenkins et al. 1986) to explain the correlation between the level of depletion and the mean line of sight density, to explore the relationship between D/H and $\langle n_H \rangle$. In this model, the interstellar medium is composed of many warm diffuse clouds, higher density cold diffuse clouds which occur with a lower spatial frequency and cold dense clouds with even lower spatial frequency. At low densities, contributions from the diffuse warm gas dominates that of the other two types of clouds. Cold diffuse clouds start to prevail with increasing densities, and at even higher densities, contributions from cold dense clouds outweigh everything else. Therefore, any correlation of a physical property with $\langle n_H \rangle$ can be attributed partly to differences of the properties of the types of clouds.

Jenkins et al. (1986) used the model developed by Spitzer (1985) to derive Equation 1, which predicts the abundance of element X_i , $A(X_i) = \log N(X_i) - \log N(H)$ ($N(H) = N(HI) + 2N(H_2)$), as a function of the sightline properties:

$$A(X_i) = A_c(X_i) + \log[1 + \frac{n_w}{\langle n_H \rangle} (\frac{\delta_w}{\delta_c} - 1)] \quad (1)$$

where $\delta_w(X_i)$ is the depletion of element X_i in the warm gas and $\delta_c(X_i)$ in the cold clouds, and n_w is the mean density of the warm gas along the line of sight

Equation 1 can be simplified to

$$A(X_i) = A_c(X_i) + \log[1 + \frac{n_w}{\langle n_H \rangle} (10^{(A_w(X_i) - A_c(X_i))} - 1)] \quad (2)$$

where $A_w(X_i)$ and $A_c(X_i)$ are the abundances of X_i in the warm diffuse medium and cold clouds, respectively. This equation assumes that diffuse cold clouds and dense cold clouds have the same level of depletion and that for $\langle n_H \rangle / n_w < 1$, all the neutral hydrogen along the line of sight is in warm gas (note that for the gas densities considered here, cold dense clouds are not expected to contribute significantly to the sightline properties, Spitzer 1985). Hence, for $\langle n_H \rangle < n_w$, $A(X_i)$ has the constant value $A_w(X_i)$, characteristic of warm gas.

Figure 19 (top panel) presents $\log(D/H)$ as a function of the average sightline density, $\langle n_H \rangle$. For comparison, we plot also $\log(O/H)$ (bottom panel). All the data have been presented previously in the top and middle panels of Figure 17 and are also listed in Table 12. Also plotted is $(D/H)_{\text{prim}} = (2.62 \pm_{0.20}^{0.18}) \times 10^{-5}$, determined from analysis of the *Wilkinson Microwave Anisotropy Probe (WMAP)* satellite data (top panel, Spergel et al. 2003) and $O/H = (3.43 \pm 0.15) \times 10^{-4}$ from Meyer et al. (1998) (bottom panel). Like Jenkins et al. (1986) we adopt $n_w = 0.10 \text{ cm}^{-3}$ below, to determine $A_w(D)$ and $A_c(D)$. As it can be seen in Figure 19, $\langle n_H \rangle = 0.10 \text{ cm}^{-3}$ seems to be a natural point, after which the scatter in D/H increases. However choosing a value in the range $0.08 < \langle n_H \rangle < 0.12$ does not affect $A_w(D)$

determined below. A non-linear least squares fit (χ^2 minimization) is used to fit $A(D)$ from Equation 2 above to the data plotted in the top panel of Figure 19.

We derive $A_w(D) = -4.80 \pm 0.01$ ($\langle n_H \rangle < 0.10 \text{ cm}^{-3}$) corresponding to $D/H = 1.58 \times 10^{-5}$ and $\chi^2_\nu = 1.2$ (26 degrees of freedom). This D/H ratio is consistent with the one derived for the LB by Wood et al. (2004), $D/H = (1.56 \pm 0.04) \times 10^{-5}$. We note however, that not all data points with $\langle n_H \rangle < 0.10 \text{ cm}^{-3}$ correspond to targets located inside the LB, although all sightlines inside the LB have $\langle n_H \rangle \leq 0.10 \text{ cm}^{-3}$. There are five sightlines of this type, outside the LB; β Cen, λ Sco, γ^2 Vel, ζ Pup, and TD1 32709. Three of these have D/H values that are consistent with the low density average but λ Sco ($D/H \times 10^5 = 0.76 \pm 0.25$) and γ^2 Vel ($D/H \times 10^5 = 2.18 \pm^{0.22}_{0.19}$) are exceptional. Thus, for low densities, as well as for higher densities, which we discuss below, some sightlines apparently defy the trends by statistically significant margins.

For $\langle n_H \rangle > 0.10 \text{ cm}^{-3}$, $A_c(D)$ is mostly affected by the five points with a high D/H ratio, i.e., $\log(D/H) > -4.8$. We derive $A_c(D) = -5.03$ ($D/H = 0.93 \times 10^{-5}$) with $\chi^2_\nu = 4.7$ (16 degrees of freedom), using all ratios corresponding to sightlines with $\langle n_H \rangle > 0.10 \text{ cm}^{-3}$ (solid line in Figure 19). If we assume that these five ratios are exceptional, corresponding to sightlines with different conditions, and remove them from our fit, we would derive $A_c(D) = -5.20$ ($D/H = 0.63 \times 10^{-5}$) with $\chi^2_\nu = 2.4$ (11 degrees of freedom). The corresponding fit is represented by a dashed-dot line in the top panel of Figure 19. This fit is now heavily dominated by a single ratio corresponding to the BD+28 4211 sightline (with a small uncertainty compared to the other sightlines). If in addition we exclude this ratio so that the fit is not dominated by one point we would derive, $A_c(D) = -5.38$ ($D/H = 0.42 \times 10^{-5}$) with $\chi^2_\nu = 1.5$ (10 degrees of freedom), represented by a dashed line in the top panel of Figure 19.

For O/H in the bottom panel of Figure 19 we derive the weighted mean of $O/H = (3.78 \pm 0.18) \times 10^{-4}$ (1 σ in the mean) for $\langle n_H \rangle < 0.1 \text{ cm}^{-3}$, with $\chi^2_\nu = 0.8$ for 11 degrees of freedom. The square-root of the weighted average variance (standard deviation) is 0.56×10^{-4} . Considering only the sightlines with $\langle n_H \rangle > 0.1 \text{ cm}^{-3}$ we derive the weighted mean $O/H = (3.41 \pm 0.15) \times 10^{-4}$ with a standard deviation of 1.40×10^{-4} and $\chi^2_\nu = 5.8$ for 14 degrees of freedom. The O/H data does not show the same trend with $\langle n_H \rangle$ as the one displayed by D/H . Recent studies have shown that oxygen is not expected to be depleted for $\langle n_H \rangle < 1.5 \text{ cm}^{-3}$ (Cartledge et al. 2004). However, the bottom panel of Figure 19 does seem to indicate that for some of the densest sightlines there is an anti-correlation between D/H and O/H , which could be an indication of astration.

Another interesting comparison is the depletion of Fe compared to that implied by Figure 19 for D. Jenkins et al. (1986) found that the abundance of Fe decreases by a factor of three from the warm gas value, by $\langle n_H \rangle = 1.0$. Figure 19 indicates a factor of two or more

decrease over the same density range for D, supporting the correlation between the values of D/H and the Fe depletion reported by Linsky et al. (2005, in prep).

Analyzing D/H as a function of the average sightline density removes the need for the three regimes displayed in Figure 17. In this picture, D/H is constant and has the same value as in the LB for $\langle n_H \rangle < 0.10 \text{ cm}^{-3}$, i. e. for sightlines dominated by warm diffuse gas, implying that D/H is constant in a broader sense than has been considered before. For $\langle n_H \rangle > 0.10 \text{ cm}^{-3}$, D/H decreases with increasing density, as more of the gas is associated with cold diffuse clouds. Considering that for other elements such as Si and Fe this has been considered as evidence of depletion of these elements into dust grains (see for e.g. Jenkins et al. 1986), then our study strongly suggests that D might also be depleted into dust grains as suggested by Draine (2004) (but see Linsky et al. 2005, in prep, for discussions on other possible explanations, such as variable astration and localized infall of metal-poor gas). However, as noted above, in both regimes there are a few sightlines which are exceptional, with high D/H ratios. It is possible that along these sightlines the conditions are such that D has either been released from the grains, does not deplete onto grains, or is only mildly depleted. Also, while there are no accurate quantitative estimates for significant production of D by local sources, the possibility of such sources cannot be entirely dismissed (see for example Mullan & Linsky 1999; Prodanović & Fields 2003). The true value of D/H in cold diffuse clouds, $A_c(D)$, is difficult to derive at this point given the small number of sightlines with high gas density. Nevertheless, it seems reasonable to estimate that in cold diffuse clouds $D/H < 0.93 \times 10^{-5}$, which is the result of our fit when all the sightlines with $\langle n_H \rangle > 0.10 \text{ cm}^{-3}$ are included in the analysis.

8. SUMMARY

We have used data obtained with *FUSE* together with archival data from *IUE* and *HST* to derive column densities and ratios of column densities along the lines of sight to WD 1034+001, BD+39 3226, and TD1 32709. The D/H derived here for two of these sightlines are not consistent at the 1σ level with the Local Bubble value; none of the D/O ratios are consistent, at the 1σ level with the Local Bubble value, and present some of the highest values in the literature. Considered along with the ratios published for other sightlines, our results reinforce the scatter in the D/H measurements and indicate that there is also scatter in the D/O ratio, implying that the high D/H ratios derived here and along other sightlines are unlikely to be due to problems with the $N(\text{HI})$ determinations. We estimate that the additional, presently unknown, systematic errors on the determination of $N(\text{HI})$ would have to be of the order of 40% of each D/H ratio, in order to bring all the D/H ratios into

agreement. Thus, our results support the idea that some sightlines in the Milky Way ISM have high D/H ratios. For sightlines with $\log N(\text{H}) > 20.7$ the O/H ratios are not consistent with a single value, and are inconsistent with the local ISM value derived by Meyer et al. (1998). The hint of anti-correlation between D/H and O/H for these sightlines could be an indication of astration.

The trend between decreasing D/H with decreasing Fe/H observed by Linsky et al. (2005, in prep) is also observed when D/O versus Fe/O are considered. These ratios are not subject to possible systematic uncertainties in the determination of $N(\text{H})$.

In order to try to understand the behavior of the deuterium abundance we performed a study of D/H versus the sightline average gas density. Our results indicate that as long as the gas probed by the sightlines is in warm diffuse clouds with $\langle n_{\text{H}} \rangle < 0.10 \text{ cm}^{-3}$ D/H seems to be constant and have the Local Bubble value. In addition, our study shows that D/H seems to decrease with increasing sightline gas density, similarly to what has been observed for other elements such as Fe and Si, which strongly supports the idea that D might be depleted into dust grains. Finally, a few sightlines do not follow the trend, but show exceptionally high D/H ratios.

This work is based on data obtained for the Guaranteed Time Team by the NASA-CNES-CSA *FUSE* mission operated by The Johns Hopkins University. Financial support to U. S. participants has been provided in part by NASA contract NAS5-32985 to Johns Hopkins University. Based on observations made with the NASA/ESA Hubble Space Telescope and the International Ultraviolet Explorer, obtained from the Data Archive at the Space Telescope Science Institute, which is operated by the Association of Universities for Research in Astronomy, Inc. under NASA contract NAS5-26555. Support for MAST for non-HST data is provided by the NASA Office of Space Science via grant NAG5-7584 and by other grants and contracts. The profile fitting procedure, Owens.f, used in this work was developed by M. Lemoine and the French *FUSE* Team. We thank Todd Tripp and Scott Friedman for their help in determining $N(\text{HI})$ from *IUE* data and W. V. Dixon for useful discussions regarding the scattered light background in the *FUSE* data. We thank also Guillaume Hébrard, Jeff Linsky, and Paule Sonnentrucker for comments that helped to improve the paper.

REFERENCES

Abgrall, H., Roueff, E., Launay, F., Roncin, J. Y., & Subtil, J. L. 1993a, A&AS, 101, 273

- . 1993b, *A&AS*, 101, 323
- Allen, M. M., Jenkins, E. B., & Snow, T. P. 1992, *ApJS*, 83, 261
- André, M. K., Oliveira, C. M., Howk, J. C., Ferlet, R., Désert, J.-M., Hébrard, G., Lacour, S., des Étangs, A. L., Vidal-Madjar, A., & Moos, H. W. 2003, *ApJ*, 591, 1000
- Asplund, M., Grevesse, N., & Sauval, J. 2004, *ArXiv Astrophysics e-prints*
- Berger, J. & Fringant, A. M. 1978, *A&A*, 64, L9
- Berger, J. & Fringant, A.-M. 1980, *A&A*, 85, 367
- Black, J. H. & Dalgarno, A. 1976, *ApJ*, 203, 132
- Bluhm, H., Marggraf, O., de Boer, K. S., Richter, P., & Heber, U. 1999, *A&A*, 352, 287
- Cartledge, S. I. B., Lauroesch, J. T., Meyer, D. M., & Sofia, U. J. 2004, *ApJ*, 613, 1037
- Crenshaw, D. M., Bruegman, O. W., Johnson, R., & Fitzurka, M. 1996, *PASP*, 108, 925
- Crinklaw, G., Federman, S. R., & Joseph, C. L. 1994, *ApJ*, 424, 748
- de Avillez, M. A. & Mac Low, M. 2002, *ApJ*, 581, 1047
- Draine, B. T. 2003, *ARA&A*, 41, 241
- Draine, B. T. 2004, in *Origin and Evolution of the Elements*, 320
- Dreizler, S. 1993, *A&A*, 273, 212
- Dring, A. R., Linsky, J., Murthy, J., Henry, R. C., Moos, W., Vidal-Madjar, A., Audouze, J., & Landsman, W. 1997, *ApJ*, 488, 760
- Ferlet, R., York, D. G., Vidal-Madjar, A., & Laurent, C. 1980, *ApJ*, 242, 576
- Friedman, S. D., Hebrard, G., Tripp, T. M., Chayer, P., & Sembach, K. R. 2005, *Astrophysical Journal*, in press
- Friedman, S. D., Howk, J. C., Chayer, P., Tripp, T. M., Hébrard, G., André, M., Oliveira, C., Jenkins, E. B., Moos, H. W., Oegerle, W. R., Sonneborn, G., Lamontagne, R., Sembach, K. R., & Vidal-Madjar, A. 2002, *ApJS*, 140, 37
- Gry, C., York, D. G., & Vidal-Madjar, A. 1985, *ApJ*, 296, 593

- Hébrard, G. 2006, in *Astrophysics in the Far Ultraviolet: Five years of discovery with FUSE*, Ed. G. Sonneborn, B. G. Andersson & Warren Moos (San Francisco: ASP) in press
- Hébrard, G., Lemoine, M., Vidal-Madjar, A., Désert, J.-M., Lecavelier des Étangs, A., Ferlet, R., Wood, B. E., Linsky, J. L., Kruk, J. W., Chayer, P., Lacour, S., Blair, W. P., Friedman, S. D., Moos, H. W., Sembach, K. R., Sonneborn, G., Oegerle, W. R., & Jenkins, E. B. 2002, *ApJS*, 140, 103
- Hébrard, G., Mallouris, C., Ferlet, R., Koester, D., Lemoine, M., Vidal-Madjar, A., & York, D. 1999, *A&A*, 350, 643
- Hébrard, G. & Moos, H. W. 2003, *ApJ*, 599, 297
- Hébrard, G., Tripp, T. M., Chayer, P., Friedman, S. D., Dupuis, J., Sonnentrucker, P., Williger, G. M., & Moos, H. W. 2005, *Astrophysical Journal*, in press
- Harris, A. W., Gry, C., & Bromage, G. E. 1984, *ApJ*, 284, 157
- Hewett, P. C., Irwin, M. J., Skillman, E. D., Foltz, C. B., Willis, J. P., Warren, S. J., & Walton, N. A. 2003, *ApJ*, 599, L37
- Hoopes, C. G., Sembach, K. R., Hébrard, G., Moos, H. W., & Knauth, D. C. 2003, *ApJ*, 586, 1094
- Hubeny, I., Hummer, D. G., & Lanz, T. 1994, *A&A*, 282, 151
- Hubeny, I. & Lanz, T. 1995, *ApJ*, 439, 875
- Jenkins, E. B. 1987, in *ASSL Vol. 134: Interstellar Processes*, 533
- Jenkins, E. B. 2004, in *Origin and Evolution of the Elements*, 339
- Jenkins, E. B., Savage, B. D., & Spitzer, L. 1986, *ApJ*, 301, 355
- Jenkins, E. B., Tripp, T. M., Woźniak, P., Sofia, U. J., & Sonneborn, G. 1999, *ApJ*, 520, 182
- Jura, M. 1982, in *Advances in Ultraviolet Astronomy*, 54
- Kirkman, D., Tytler, D., Suzuki, N., O’Meara, J. M., & Lubin, D. 2003, *ApJS*, 149, 1
- Kruk, J. W., Howk, J. C., André, M., Moos, H. W., Oegerle, W. R., Oliveira, C., Sembach, K. R., Chayer, P., Linsky, J. L., Wood, B. E., Ferlet, R., Hébrard, G., Lemoine, M., Vidal-Madjar, A., & Sonneborn, G. 2002, *ApJS*, 140, 19
- Laurent, C., Vidal-Madjar, A., & York, D. G. 1979, *ApJ*, 229, 923

- Lehner, N., Gry, C., Sembach, K. R., Hébrard, G., Chayer, P., Moos, H. W., Howk, J. C., & Désert, J.-M. 2002, *ApJS*, 140, 81
- Lemke, M. 1997, *A&AS*, 122, 285
- Lemoine, M., Vidal-Madjar, A., Hébrard, G., Désert, J.-M., Ferlet, R., Lecavelier des Étangs, A., Howk, J. C., André, M., Blair, W. P., Friedman, S. D., Kruk, J. W., Lacour, S., Moos, H. W., Sembach, K., Chayer, P., Jenkins, E. B., Koester, D., Linsky, J. L., Wood, B. E., Oegerle, W. R., Sonneborn, G., & York, D. G. 2002, *ApJS*, 140, 67
- Levshakov, S. A., Dessauges-Zavadsky, M., D’Odorico, S., & Molaro, P. 2002, *ApJ*, 565, 696
- Linsky, J. L. 1998, *Space Science Reviews*, 84, 285
- Linsky, J. L., Diplas, A., Wood, B. E., Brown, A., Ayres, T. R., & Savage, B. D. 1995, *ApJ*, 451, 335
- Meyer, D. M., Cardelli, J. A., & Sofia, U. J. 1997, *ApJ*, 490, L103
- Meyer, D. M., Jura, M., & Cardelli, J. A. 1998, *ApJ*, 493, 222
- Moos, H. W., Cash, W. C., Cowie, L. L., Davidsen, A. F., Dupree, A. K., Feldman, P. D., Friedman, S. D., Green, J. C., Green, R. F., Gry, C., Hutchings, J. B., Jenkins, E. B., Linsky, J. L., Malina, R. F., Michalitsianos, A. G., Savage, B. D., Shull, J. M., Siegmund, O. H. W., Snow, T. P., Sonneborn, G., Vidal-Madjar, A., Willis, A. J., Woodgate, B. E., York, D. G., Ake, T. B., Andersson, B.-G., Andrews, J. P., Barkhouser, R. H., Bianchi, L., Blair, W. P., Brownsberger, K. R., Cha, A. N., Chayer, P., Conard, S. J., Fullerton, A. W., Gaines, G. A., Grange, R., Gummin, M. A., Hebrard, G., Kriss, G. A., Kruk, J. W., Mark, D., McCarthy, D. K., Morbey, C. L., Murowinski, R., Murphy, E. M., Oegerle, W. R., Ohl, R. G., Oliveira, C., Osterman, S. N., Sahnou, D. J., Saisse, M., Sembach, K. R., Weaver, H. A., Welsh, B. Y., Wilkinson, E., & Zheng, W. 2000, *ApJ*, 538, L1
- Moos, H. W., Sembach, K. R., Vidal-Madjar, A., York, D. G., Friedman, S. D., Hébrard, G., Kruk, J. W., Lehner, N., Lemoine, M., Sonneborn, G., Wood, B. E., Ake, T. B., André, M., Blair, W. P., Chayer, P., Gry, C., Dupree, A. K., Ferlet, R., Feldman, P. D., Green, J. C., Howk, J. C., Hutchings, J. B., Jenkins, E. B., Linsky, J. L., Murphy, E. M., Oegerle, W. R., Oliveira, C., Roth, K., Sahnou, D. J., Savage, B. D., Shull, J. M., Tripp, T. M., Weiler, E. J., Welsh, B. Y., Wilkinson, E., & Woodgate, B. E. 2002, *ApJS*, 140, 3
- Morton, D. C. 1974, *ApJ*, 193, L35

—. 2003, *ApJS*, 149, 205

Mullan, D. J. & Linsky, J. L. 1999, *ApJ*, 511, 502

Oegerle, W. R., Jenkins, E. B., Shelton, R. L., Bowen, D. V., & Chayer, P. 2005, *ApJ*, 622, 377

Oliveira, C. M., Dupuis, J., Chayer, P., & Moos, H. W. 2005, *ApJ*, 625, 232

Oliveira, C. M., Hébrard, G., Howk, J. C., Kruk, J. W., Chayer, P., & Moos, H. W. 2003, *ApJ*, 587, 235

O’Meara, J. M., Tytler, D., Kirkman, D., Suzuki, N., Prochaska, J. X., Lubin, D., & Wolfe, A. M. 2001, *ApJ*, 552, 718

Pettini, M. & Bowen, D. V. 2001, *ApJ*, 560, 41

Piskunov, N., Wood, B. E., Linsky, J. L., Dempsey, R. C., & Ayres, T. R. 1997, *ApJ*, 474, 315

Prochaska, J. X., Tripp, T. M., & Howk, J. C. 2005, *ApJ*, 620, L39

Prodanović, T. & Fields, B. D. 2003, *ApJ*, 597, 48

Rauch, T., Kerber, F., & Pauli, E.-M. 2004, *A&A*, 417, 647

Rogerson, J. B. & York, D. G. 1973, *ApJ*, 186, L95

Sahnow, D. J., Moos, H. W., Ake, T. B., Andersen, J., Andersson, B.-G., Andre, M., Artis, D., Berman, A. F., Blair, W. P., Brownsberger, K. R., Calvani, H. M., Chayer, P., Conard, S. J., Feldman, P. D., Friedman, S. D., Fullerton, A. W., Gaines, G. A., Gawne, W. C., Green, J. C., Gummin, M. A., Jennings, T. B., Joyce, J. B., Kaiser, M. E., Kruk, J. W., Lindler, D. J., Massa, D., Murphy, E. M., Oegerle, W. R., Ohl, R. G., Roberts, B. A., Romelfanger, M. L., Roth, K. C., Sankrit, R., Sembach, K. R., Shelton, R. L., Siegmund, O. H. W., Silva, C. J., Sonneborn, G., Vaclavik, S. R., Weaver, H. A., & Wilkinson, E. 2000, *ApJ*, 538, L7

Savage, B. D. & Bohlin, R. C. 1979, *ApJ*, 229, 136

Sembach, K. R., Wakker, B. P., Tripp, T. M., Richter, P., Kruk, J. W., Blair, W. P., Moos, H. W., Savage, B. D., Shull, J. M., York, D. G., Sonneborn, G., Hébrard, G., Ferlet, R., Vidal-Madjar, A., Friedman, S. D., & Jenkins, E. B. 2004, *ApJS*, 150, 387

Sfeir, D. M., Lallement, R., Crifo, F., & Welsh, B. Y. 1999, *A&A*, 346, 785

- Sion, E. M., Liebert, J., & Wesemael, F. 1985, *ApJ*, 292, 477
- Sonneborn, G., André, M., Oliveira, C., Hébrard, G., Howk, J. C., Tripp, T. M., Chayer, P., Friedman, S. D., Kruk, J. W., Jenkins, E. B., Lemoine, M., Moos, H. W., Oegerle, W. R., Sembach, K. R., & Vidal-Madjar, A. 2002, *ApJS*, 140, 51
- Sonneborn, G., Tripp, T. M., Ferlet, R., Jenkins, E. B., Sofia, U. J., Vidal-Madjar, A., & Woźniak, P. . R. 2000, *ApJ*, 545, 277
- Spiegel, D. N., Verde, L., Peiris, H. V., Komatsu, E., Nolte, M. R., Bennett, C. L., Halpern, M., Hinshaw, G., Jarosik, N., Kogut, A., Limon, M., Meyer, S. S., Page, L., Tucker, G. S., Weiland, J. L., Wollack, E., & Wright, E. L. 2003, *ApJS*, 148, 175
- Spitzer, L. 1985, *ApJ*, 290, L21
- Vennes, S., Polonski, E. F., Lanz, T., Thorstensen, J. R., Chayer, P., & Gull, T. R. 2000, *ApJ*, 544, 423
- Vidal, C. R., Cooper, J., & Smith, E. W. 1973, *ApJS*, 25, 37
- Werner, K., Dreizler, S., & Wolff, B. 1995, *A&A*, 298, 567
- Williger, G. M., Oliveira, C., Hébrard, G., Dupuis, J., Dreizler, S., & Moos, H. W. 2005, *ApJ* in press
- Wood, B. E., Alexander, W. R., & Linsky, J. L. 1996, *ApJ*, 470, 1157
- Wood, B. E., Linsky, J. L., Hébrard, G., Vidal-Madjar, A., Lemoine, M., Moos, H. W., Sembach, K. R., & Jenkins, E. B. 2002a, *ApJS*, 140, 91
- Wood, B. E., Linsky, J. L., Hébrard, G., Williger, G. M., Moos, H. W., & Blair, W. P. 2004, *ApJ*, 609, 838
- Wood, B. E., Linsky, J. L., & Zank, G. P. 2000, *ApJ*, 537, 304
- Wood, B. E., Redfield, S., Linsky, J. L., & Sahu, M. S. 2002b, *ApJ*, 581, 1168
- York, D. G. 1983, *ApJ*, 264, 172
- York, D. G. & Kinahan, B. F. 1979, *ApJ*, 228, 127
- York, D. G. & Rogerson, J. B. 1976, *ApJ*, 203, 378

Table 1. Stellar Properties

Star	T_{eff} (K)	$\log g$ (cm^{-2})	d (pc)	l ($^{\circ}$)	b ($^{\circ}$)	Sp. Type	$v_{\text{PH}} - v_{\text{ISM}}$ (km s^{-1})
WD 1034+001 ^a	$100,000 \pm \frac{15,000}{10,000}$	7.5 ± 0.3	$155 \pm \frac{58}{43}$	247.55	+47.75	DO	$\sim +50$
BD+39 3226 ^b	45,000	5.5	$290 \pm \frac{140}{70}$	65.00	+28.77	sdO	~ -255
TD1 32709 ^c	$46,500 \pm 1,000$	5.55 ± 0.15	520 ± 90	232.98	+28.12	sdO	$\sim -13^{\text{d}}$

^aFrom Werner et al. (1995).

^bFrom Bluhm et al. (1999).

^cFrom Dreizler (1993).

^dThis work.

Table 2. Log of *FUSE* observations

Star	Program ID	Aperture	Mode	Time (Ks)	Date	CalFUSE
WD 1034+001	P1042003	MDRS	TTAG	6.7	2004 April 04	2.4.2
BD+39 3226	P3020501	MDRS	HIST	5.2	2004 May 21	2.4.2
TD1 32709	P2051301	MDRS	HIST	1.8	2004 March 12	2.4.1
	P2051302	MDRS	HIST	3.2	2004 May 4	2.4.1
	P2051303	MDRS	HIST	2.4	2004 May 5	2.4.1

Table 3. Atomic data and analysis methods for the lines used in the analyses^a

Species	Wavelength (Å)	Log $f\lambda$	WD 1034+001	BD+39 3226	TD1 32709
HI	1215.670	2.70	P	...	P
DI	916.1785	−0.28	P	...	P
...	917.8797	−0.07	A, P
...	919.1013	0.04	A, C, P	A, C, P	A, C, P
...	920.713	0.17	A, C, P	C, P	A, C, P
...	922.899	0.31	A, C, P	...	C
...	925.974	0.47	C, P	C, P	C, P
...	930.495	0.65	C, P
...	937.548	0.86	C	C	C, P
...	949.485	1.12	...	C	C
...	972.272	1.45	C	C	C
CH	1036.3367	2.09	B/S	A	A
CH*	1037.018	2.11	A	A	A
CH	977.0200	2.87	A	A	B/S
NI	951.2948	−1.66	P
...	952.303	0.25	C	C	C
...	952.415	0.21	...	C	C
...	952.523	−0.24	A, C, P	A, C, P	A, C, P
...	953.415	1.10	C	C	C
...	953.655	1.38	C	C	C
...	953.9699	1.52	C	C	...
...	954.1042	0.81	C	C	C
...	955.8819	−1.54	P
...	959.4937	−1.30	P
...	963.990	1.54	C	C	C
...	964.626	0.96	C	C	C
...	1134.1653	1.69	C	C	C
...	1134.4149	1.53	C	C	C
...	1134.9803	1.24	C
NI	1083.994	2.10	A	A	A
OI	916.8150	−0.36	C

Table 3—Continued

Species	Wavelength (Å)	Log $f\lambda$	WD 1034+001	BD+39 3226	TD1 32709
...	919.658	−0.06	C	C	C
...	919.917	−0.79	A, P	A, C, P	A, C, P
...	921.875	0.04	C
...	922.200	−0.65	P	...	P
...	924.950	0.15	C	C	...
...	925.446	−0.49	A, C	A, C	C
...	929.5168	0.32	C
...	930.257	−0.30	C	C	C
...	936.6295	0.53	...	C	C
...	948.6855	0.77	C
...	950.885	0.18	C	C	...
...	971.738	1.13	...	C	C
...	974.070	−1.82	P, C	...	P, C
...	976.4481	0.51	C
...	1039.2301	0.98	C
O VI	1031.9261	2.13	P	P	B/S
...	1037.6167	1.83	P	...	B/S
Si II	1020.699	1.22	A	A	A
P II	1152.8180	2.45	A	A	A
S III	1012.4950	1.65	A
S IV	1062.6780	1.64	A
Ar I	1048.220	2.44	A	A	A
Fe II	1055.2617	0.90	...	A, C, P	...
...	1063.176	1.76	C	C	C, P
...	1081.9352	−0.90	C, P	P	C
...	1096.8770	1.55	C, P	C, P	P
...	1112.0480	0.84	C, P	P	C
...	1121.975	1.36	C, P	C, P	...
...	1125.448	1.26	...	C, P	...
...	1133.6654	0.80	A, C, P	C, P	A, C, P
...	1142.3656	0.68	P	...	C

Table 3—Continued

Species	Wavelength (Å)	Log $f\lambda$	WD 1034+001	BD+39 3226	TD1 32709
...	1143.2260	1.31	C, P	C, P	A, C, P
...	1144.938	2.08	C, P	C	...

^aA, C, and P, denote lines that are analyzed with apparent optical depth, curve of growth, and profile fitting techniques, respectively. B/S means that no column densities were derived from these lines due to blending with stellar features.

Table 4. Equivalent widths of the atomic lines used with the COG method (mÅ)

Species	Wavelength (Å)	WD 1034+001	BD+39 3226	TD1 32709
DI	919.1013	16.96 ± 2.46	12.85 ± 2.72	6.46 ± 4.23
...	920.713	18.68 ± 2.44	14.68 ± 3.77	18.59 ± 2.23
...	922.899	27.49 ± 3.47	...	26.93 ± 5.13
...	925.974	39.78 ± 3.00	26.78 ± 2.60	26.29 ± 4.33
...	930.495	41.78 ± 3.10
...	937.548	46.06 ± 4.42	34.77 ± 3.06	48.31 ± 6.60
...	949.485	...	53.68 ± 2.88	53.61 ± 5.80
...	972.272	67.64 ± 8.91	71.00 ± 4.91	74.34 ± 6.52
NI	952.303	62.29 ± 3.43	37.71 ± 1.68	61.98 ± 3.17
...	952.415	...	44.11 ± 1.59	49.23 ± 2.52
...	952.523	19.40 ± 2.71	21.96 ± 1.52	29.63 ± 2.82
...	953.415	67.19 ± 3.58	54.64 ± 2.05	70.61 ± 3.48
...	953.655	75.78 ± 3.84	63.32 ± 2.51	81.25 ± 3.53
...	953.9699	78.27 ± 3.54	65.91 ± 2.14	...
...	954.1042	68.76 ± 3.49	51.17 ± 1.86	57.25 ± 3.59
...	963.990	67.68 ± 4.73	77.37 ± 2.54	70.22 ± 3.19
...	964.626	66.84 ± 4.10	64.60 ± 2.50	59.59 ± 3.37
...	1134.1653	84.50 ± 2.76	73.40 ± 1.31	101.82 ± 2.35
...	1134.4149	86.95 ± 2.48	81.27 ± 1.41	107.53 ± 2.57
...	1134.9803	97.89 ± 2.01
OI	916.8150	48.33 ± 3.92
...	919.658	56.28 ± 3.32	44.98 ± 2.57	44.90 ± 3.31
...	919.917	...	18.63 ± 1.47	27.62 ± 2.91
...	921.875	59.46 ± 3.33
...	924.950	66.17 ± 3.59	57.68 ± 2.53	...
...	925.446	44.46 ± 3.37	39.13 ± 2.14	41.62 ± 2.88
...	929.5168	72.33 ± 3.22
...	930.257	54.78 ± 3.54	41.69 ± 2.11	50.04 ± 3.72
...	936.6295	...	70.93 ± 2.69	85.04 ± 3.10
...	948.6855	88.06 ± 3.87
...	950.885	64.30 ± 3.76	54.69 ± 1.75	...

Table 4—Continued

Species	Wavelength (Å)	WD 1034+001	BD+39 3226	TD1 32709
...	971.738	...	90.73 ± 3.24	84.34 ± 5.02
...	974.070	4.86 ± 2.06	...	6.91 ± 1.91
...	976.4481	74.83 ± 3.26
...	1039.2301	101.94 ± 1.88
Fe II	1055.2617	...	8.29 ± 0.94	...
...	1063.176	54.53 ± 2.81	41.14 ± 1.28	26.09 ± 1.23
...	1081.9352	21.03 ± 3.90	...	8.00 ± 1.64
...	1096.8770	21.03 ± 1.75	34.52 ± 1.43	...
...	1112.0480	11.19 ± 1.52	...	5.87 ± 1.05
...	1121.975	22.58 ± 2.07	14.14 ± 0.91	...
...	1125.448	...	22.41 ± 1.09	...
...	1133.6654	5.70 ± 1.90	6.48 ± 0.64	5.28 ± 1.01
...	1142.3656	5.84 ± 0.94
...	1143.2260	16.01 ± 1.92	22.98 ± 1.06	16.43 ± 1.47
...	1144.938	55.82 ± 2.48	57.39 ± 1.34	...

Table 5. H₂ Column Densities (Log)

H ₂	WD 1034+001	BD+39 3226	TD1 32709
$J = 0$	14.55 ± 0.10	15.17 ± 0.15	13.50 ± 0.15
$J = 1$	15.63 ± 0.15	$15.41 \pm {}^{0.06}_{0.10}$	14.35 ± 0.15
$J = 2$	14.60 ± 0.10	14.47 ± 0.10	13.44 ± 0.15
$J = 3$	14.30 ± 0.10	13.95 ± 0.10	13.33 ± 0.15
$J = 4$...	13.38 ± 0.10	...
$J = 5$...	13.49 ± 0.07	...
Total	$15.72 \pm {}^{0.13}_{0.12}$	$15.65 \pm {}^{0.06}_{0.07}$	$14.48 \pm {}^{0.12}_{0.11}$

Table 6. Column Densities (Log) Along the WD 1034+001 Sightline

Species	AOD	COG	PF
D I	$15.27 \pm {}^{0.11}_{0.14} (\lambda 919)$	$15.40 \pm {}^{0.07}_{0.06}$	$15.40 \pm {}^{0.05}_{0.03}$
N I	$15.89 \pm {}^{0.08}_{0.09} (\lambda 952.5)$	$16.07 \pm {}^{0.22}_{0.14}$	$15.84 \pm {}^{0.12}_{0.13}$
O I	$16.57 \pm 0.07 (\lambda 919.9)$	16.62 ± 0.05	$16.57 \pm {}^{0.07}_{0.08}$
Fe II	$14.19 \pm {}^{0.11}_{0.15} (\lambda 1133)$	$14.14 \pm {}^{0.11}_{0.10}$	$14.05 \pm {}^{0.05}_{0.03}$

Note. — The transitions associated with the AOD results quoted in the table are given in (). Uncertainties are 1σ .

Table 7. Column Densities (Log) Along the BD+39 3226 Sightline

Species	AOD	COG	PF
D I	$15.27 \pm {}^{0.08}_{0.11} (\lambda 919)$	$15.15 \pm {}^{0.08}_{0.07}$	$15.15 \pm {}^{0.04}_{0.03}$
N I	$15.93 \pm {}^{0.12}_{0.17} (\lambda 952.5)$	$15.88 \pm {}^{0.11}_{0.09}$	$15.80 \pm {}^{0.06}_{0.05}$
O I	$16.33 \pm 0.08 (\lambda 919.9)$	$16.31 \pm {}^{0.07}_{0.06}$	16.51 ± 0.04
Fe II	$14.05 \pm 0.05 (\lambda 1055)$	$14.13 \pm {}^{0.06}_{0.05}$	14.21 ± 0.02

Note. — The transitions associated with the AOD results quoted in the table are given in (). Uncertainties are 1σ .

Table 8. Column Densities (Log) Along the TD1 32709 Sightline

Species	AOD	COG	PF
D I	$15.33 \pm_{0.09}^{0.08} (\lambda 919)$	$15.29 \pm_{0.04}^{0.05}$	15.26 ± 0.03
N I	$15.93 \pm 0.04 (\lambda 952.5)$	$16.02 \pm_{0.12}^{0.16}$	$15.97 \pm_{0.11}^{0.09}$
O I	$16.36 \pm_{0.08}^{0.07} (\lambda 919.9)$	$16.45 \pm_{0.03}^{0.09}$	$16.48 \pm_{0.05}^{0.06}$
Fe II	$13.98 \pm_{0.10}^{0.08} (\lambda 1133)$	14.03 ± 0.05	$13.87 \pm_{0.02}^{0.03}$

Note. — The transitions associated with the AOD results quoted in the table are given in (). Uncertainties are 1σ .

Table 9. Atomic Column Densities (Log)

Species	WD 1034+001	BD+39 3226	TD1 32709
H I	20.07 ± 0.07	20.08 ± 0.09^a	20.03 ± 0.10
DI	15.40 ± 0.07	15.15 ± 0.05	15.30 ± 0.05
C II	blend	≥ 14.24	≥ 14.65
C II*	≥ 13.88	≥ 13.63	≥ 13.94
C III	≥ 13.66	≥ 13.40	blend
NI	15.96 ± 0.12	15.85 ± 0.10	15.98 ± 0.10
N II	≥ 14.15	≥ 14.25	$\geq 14.35^b$
O I	16.60 ± 0.10	16.40 ± 0.10	16.42 ± 0.10
O VI	13.08 ± 0.08^c	13.14 ± 0.05	...
Si II	≥ 14.68	≥ 14.58	≥ 14.66
P II	≥ 13.16	≥ 13.01	≥ 13.19
S III	$\geq 14.17^c$
S IV	$\geq 14.08^c$
Ar I	≥ 13.65	≥ 13.45	≥ 13.64
Fe II	14.10 ± 0.10	14.15 ± 0.07	13.95 ± 0.10

^aFrom Bluhm et al. (1999).

^bPossibly contaminated by stellar N II absorption.

^cCircumstellar contribution possible, see §4.2.1.

Table 10. Ratios of Column Densities

Ratio	WD 1034+001	BD+39 3226	TD1 32709
(DI/HI) $\times 10^5$	$2.14 \pm \begin{smallmatrix} 0.53 \\ 0.45 \end{smallmatrix}$	$1.17 \pm \begin{smallmatrix} 0.31 \\ 0.25 \end{smallmatrix}$	$1.86 \pm \begin{smallmatrix} 0.53 \\ 0.43 \end{smallmatrix}$
(NI/HI) $\times 10^5$	$7.76 \pm \begin{smallmatrix} 2.82 \\ 2.20 \end{smallmatrix}$	$5.89 \pm \begin{smallmatrix} 2.04 \\ 1.63 \end{smallmatrix}$	$8.91 \pm \begin{smallmatrix} 3.26 \\ 2.59 \end{smallmatrix}$
(OI/HI) $\times 10^4$	$3.39 \pm \begin{smallmatrix} 1.06 \\ 0.86 \end{smallmatrix}$	$2.09 \pm \begin{smallmatrix} 0.72 \\ 0.58 \end{smallmatrix}$	$2.45 \pm \begin{smallmatrix} 0.90 \\ 0.71 \end{smallmatrix}$
(DI/OI) $\times 10^2$	$6.31 \pm \begin{smallmatrix} 1.79 \\ 1.38 \end{smallmatrix}$	$5.62 \pm \begin{smallmatrix} 1.61 \\ 1.31 \end{smallmatrix}$	$7.59 \pm \begin{smallmatrix} 2.17 \\ 1.76 \end{smallmatrix}$
(DI/NI) $\times 10^1$	$2.75 \pm \begin{smallmatrix} 1.00 \\ 0.78 \end{smallmatrix}$	$2.00 \pm \begin{smallmatrix} 0.57 \\ 0.46 \end{smallmatrix}$	$2.09 \pm \begin{smallmatrix} 0.60 \\ 0.49 \end{smallmatrix}$
OI/NI	$4.37 \pm \begin{smallmatrix} 1.79 \\ 1.38 \end{smallmatrix}$	$3.55 \pm \begin{smallmatrix} 1.30 \\ 1.03 \end{smallmatrix}$	$2.75 \pm \begin{smallmatrix} 1.01 \\ 0.80 \end{smallmatrix}$

Table 11. BD+39 3226: N_{FUSE} vs. $N_{ORFEUS+IUE}$

Species	$\log N_{FUSE}^a$	$\log N_{ORFEUS+IUE}^b$
D I	15.15 ± 0.05	15.16 ± 0.13
C	≥ 14.38	16.40 ± 0.75
NI	15.85 ± 0.10	14.75 ± 0.25
O I	16.40 ± 0.10	$16.40 \pm \begin{smallmatrix} 0.75 \\ 0.50 \end{smallmatrix}$
Si	≥ 14.58	14.80 ± 0.20
Fe II	14.15 ± 0.07	14.10 ± 0.15
H ₂ ($J = 0$)	15.17 ± 0.15	15.10 ± 0.20
... ($J = 1$)	$15.41 \pm \begin{smallmatrix} 0.06 \\ 0.10 \end{smallmatrix}$	$15.50 \pm \begin{smallmatrix} 0.20 \\ 0.30 \end{smallmatrix}$
... ($J = 2$)	14.47 ± 0.10	$14.10 \pm \begin{smallmatrix} 0.15 \\ 0.20 \end{smallmatrix}$
... ($J = 3$)	13.95 ± 0.10	$13.95 \pm \begin{smallmatrix} 0.15 \\ 0.10 \end{smallmatrix}$
... ($J = 4$)	13.38 ± 0.10	$13.80 \pm \begin{smallmatrix} 0.30 \\ 0.20 \end{smallmatrix}$
... ($J = 5$)	13.49 ± 0.07	< 13.40

^aThis work.

^bBluhm et al. (1999). No f -value corrections were applied to N .

Table 12. Compilation of Sightline Ratios

Star	d (pc)	$\log N(\text{H})$	$(\text{D}/\text{H}) \times 10^5$	$(\text{D}/\text{O}) \times 10^2$	$(\text{O}/\text{H}) \times 10^4$	$\langle n_{\text{H}} \rangle$ (cm^{-3})	Ref.
Sirius B	2.64	17.81 ± 0.11	1.17 ± 0.37	3.9 ± 0.8	$3.02 \pm \begin{smallmatrix} 0.95 \\ 0.75 \end{smallmatrix}$	0.079	2, 2, 1
ϵ Eri	3.22	17.88 ± 0.04	1.40 ± 0.20	0.076	3, 3, -
Procyon	3.50	18.06 ± 0.05	1.60 ± 0.20	0.106	4
ϵ Ind	3.63	18.00 ± 0.05	1.60 ± 0.20	0.089	5
36 Oph	5.99	17.85 ± 0.08	1.50 ± 0.25	0.038	6
β Gem	10.34	18.26 ± 0.04	1.47 ± 0.20	0.057	3, 3, -
Capella	12.9	18.24 ± 0.04	$1.60 \pm \begin{smallmatrix} 0.14 \\ 0.19 \end{smallmatrix}$	2.6 ± 1.2	$6.31 \pm \begin{smallmatrix} 3.69 \\ 1.95 \end{smallmatrix}$	0.044	4, 4, 7
β Cas	16.7	18.13 ± 0.03	1.70 ± 0.15	0.026	3
α Tri	19.7	18.33 ± 0.04	1.32 ± 0.30	0.035	3
λ And	25.8	18.45 ± 0.08	1.70 ± 0.25	0.035	7
β Cet	29.4	18.36 ± 0.05	2.20 ± 0.55	0.025	8
HR 1099	29	18.13 ± 0.02	1.46 ± 0.09	0.015	8
σ Gem	37	18.20 ± 0.04	1.36 ± 0.20	0.014	3
WD 1634–573	37	18.85 ± 0.06	1.60 ± 0.25	3.5 ± 0.3	4.57 ± 0.75	0.062	9
WD 2211–495	53	18.76 ± 0.15	1.51 ± 0.60	4.0 ± 0.6	$3.80 \pm \begin{smallmatrix} 1.61 \\ 1.16 \end{smallmatrix}$	0.035	10
HZ 43	68	17.93 ± 0.03	1.66 ± 0.14	4.6 ± 0.5	$3.63 \pm \begin{smallmatrix} 0.44 \\ 0.70 \end{smallmatrix}$	0.004	11
G191–B2B	69	18.18 ± 0.09	1.66 ± 0.45	3.5 ± 0.4	$4.79 \pm \begin{smallmatrix} 1.19 \\ 0.99 \end{smallmatrix}$	0.007	12
Feige 24	74	18.47 ± 0.03	1.30 ± 0.50	3.9 ± 1.7	$3.33 \pm \begin{smallmatrix} 0.59 \\ 0.56 \end{smallmatrix}$	0.013	13, 13, 14
WD 0621–376	78	18.70 ± 0.15	1.41 ± 0.56	3.9 ± 0.6	$3.63 \pm \begin{smallmatrix} 1.56 \\ 1.10 \end{smallmatrix}$	0.021	15
GD 246	79	19.11 ± 0.03	$1.51 \pm \begin{smallmatrix} 0.20 \\ 0.17 \end{smallmatrix}$	4.2 ± 0.6	$3.63 \pm \begin{smallmatrix} 0.44 \\ 0.34 \end{smallmatrix}$	0.053	16
α Vir	80	19.00 ± 0.10	$1.58 \pm \begin{smallmatrix} 1.01 \\ 0.46 \end{smallmatrix}$	4.2 ± 2.0	$3.80 \pm \begin{smallmatrix} 1.39 \\ 1.11 \end{smallmatrix}$	0.041	17, 17, 18
31 Com	94	17.88 ± 0.03	2.00 ± 0.20	0.003	3

Table 12—Continued

Star	d (pc)	$\log N(\text{H})$	$(\text{D}/\text{H}) \times 10^5$	$(\text{D}/\text{O}) \times 10^2$	$(\text{O}/\text{H}) \times 10^4$	$\langle n_{\text{H}} \rangle$ (cm^{-3})	Ref.
α Cru	98	19.60 ± 0.10	$2.24 \pm \begin{smallmatrix} 0.64 \\ 0.52 \end{smallmatrix}$	0.132	17, 17, -
BD+28 4211	104	19.85 ± 0.02	1.26 ± 0.08	4.7 ± 0.4	$2.69 \pm \begin{smallmatrix} 0.23 \\ 0.22 \end{smallmatrix}$	0.221	19, 1, 1
θ Car	135	20.28 ± 0.10	0.50 ± 0.16	0.457	20
β Cma	153	18.20 ± 0.16	$1.20 \pm \begin{smallmatrix} 1.10 \\ 0.50 \end{smallmatrix}$	0.003	21
WD 1034+001	155	20.07 ± 0.07	$2.14 \pm \begin{smallmatrix} 0.53 \\ 0.45 \end{smallmatrix}$	$6.31 \pm \begin{smallmatrix} 1.79 \\ 1.38 \end{smallmatrix}$	$3.39 \pm \begin{smallmatrix} 1.06 \\ 0.86 \end{smallmatrix}$	0.246	22
β Cen	161	19.54 ± 0.05	$1.26 \pm \begin{smallmatrix} 1.25 \\ 0.45 \end{smallmatrix}$	0.070	17
Feige 110	179	20.14 ± 0.09	2.14 ± 0.41	2.6 ± 0.5	$8.32 \pm \begin{smallmatrix} 2.41 \\ 1.99 \end{smallmatrix}$	0.245	23, 23, 35
γ Cas	188	20.04 ± 0.04	1.12 ± 0.25	2.5 ± 0.4	$5.25 \pm \begin{smallmatrix} 0.72 \\ 0.35 \end{smallmatrix}$	0.189	24, 24, 25
λ Sco	216	19.23 ± 0.03	0.76 ± 0.25	$1.8 \pm \begin{smallmatrix} 0.4 \\ 0.3 \end{smallmatrix}$	$4.24 \pm \begin{smallmatrix} 0.38 \\ 0.31 \end{smallmatrix}$	0.026	26
γ^2 Vel	258	19.71 ± 0.03	$2.18 \pm \begin{smallmatrix} 0.22 \\ 0.19 \end{smallmatrix}$	0.064	27, 27, -
δ Ori	281	20.19 ± 0.03	$0.74 \pm \begin{smallmatrix} 0.12 \\ 0.09 \end{smallmatrix}$	2.5 ± 0.4	2.80 ± 0.40	0.179	28, 28, 25
BD+39 3226	290	20.08 ± 0.09	$1.17 \pm \begin{smallmatrix} 0.31 \\ 0.25 \end{smallmatrix}$	$5.62 \pm \begin{smallmatrix} 1.61 \\ 1.31 \end{smallmatrix}$	$2.09 \pm \begin{smallmatrix} 0.72 \\ 0.58 \end{smallmatrix}$	0.134	29, 22, 22
PG 0038+199	297	20.48 ± 0.04	$1.91 \pm \begin{smallmatrix} 0.26 \\ 0.24 \end{smallmatrix}$	$2.4 \pm \begin{smallmatrix} 1.0 \\ 0.5 \end{smallmatrix}$	$7.76 \pm \begin{smallmatrix} 1.78 \\ 2.33 \end{smallmatrix}$	0.330	30
ι Ori	407	20.16 ± 0.10	$1.40 \pm \begin{smallmatrix} 0.50 \\ 1.00 \end{smallmatrix}$	3.5 ± 0.8	$3.98 \pm \begin{smallmatrix} 1.38 \\ 1.11 \end{smallmatrix}$	0.115	31, 31, 25
ϵ Ori	412	20.40 ± 0.08	0.65 ± 0.30	1.9 ± 0.3	$3.80 \pm \begin{smallmatrix} 0.90 \\ 0.76 \end{smallmatrix}$	0.198	31, 31, 25
ζ Pup	429	19.96 ± 0.03	$1.42 \pm \begin{smallmatrix} 0.15 \\ 0.14 \end{smallmatrix}$	0.069	27
TD1 32709	520	20.03 ± 0.10	$1.86 \pm \begin{smallmatrix} 0.53 \\ 0.43 \end{smallmatrix}$	$7.59 \pm \begin{smallmatrix} 2.17 \\ 1.76 \end{smallmatrix}$	$2.45 \pm \begin{smallmatrix} 0.90 \\ 0.71 \end{smallmatrix}$	0.067	22
LSE 44	554	$20.52 \pm \begin{smallmatrix} 0.11 \\ 0.14 \end{smallmatrix}$	$2.24 \pm \begin{smallmatrix} 0.70 \\ 0.67 \end{smallmatrix}$	$1.99 \pm \begin{smallmatrix} 0.65 \\ 0.34 \end{smallmatrix}$	$11.3 \pm \begin{smallmatrix} 4.8 \\ 3.6 \end{smallmatrix}$	0.194	32
LS 1274	580	20.98 ± 0.04	0.76 ± 0.18	1.8 ± 0.5	$4.68 \pm \begin{smallmatrix} 1.05 \\ 0.81 \end{smallmatrix}$	0.534	33, 33, 1
JL 9	590	20.78 ± 0.05	1.00 ± 0.19	1.9 ± 0.8	$5.25 \pm \begin{smallmatrix} 3.14 \\ 1.47 \end{smallmatrix}$	0.331	33
HD 195965	794	20.95 ± 0.03	$0.85 \pm \begin{smallmatrix} 0.17 \\ 0.12 \end{smallmatrix}$	1.3 ± 0.3	$6.61 \pm \begin{smallmatrix} 0.52 \\ 0.56 \end{smallmatrix}$	0.364	34
HD 191877	2200	21.05 ± 0.05	$0.78 \pm \begin{smallmatrix} 0.26 \\ 0.13 \end{smallmatrix}$	2.5 ± 1.0	$3.09 \pm \begin{smallmatrix} 0.99 \\ 0.49 \end{smallmatrix}$	0.165	34
HD 90087	2740	21.17 ± 0.05	0.98 ± 0.19	1.7 ± 0.4	5.8 ± 1.0	0.175	35

Table 12—Continued

Star	d (pc)	$\log N(\text{H})$	$(\text{D}/\text{H}) \times 10^5$	$(\text{D}/\text{O}) \times 10^2$	$(\text{O}/\text{H}) \times 10^4$	$\langle n_{\text{H}} \rangle$ (cm^{-3})	Ref.
WD 2004–605	52	19.11	...	4.8 ± 1.3	1
WD 1631+781	67	19.36	...	3.8 ± 1.2	1
WD 2331–475	82	18.94	...	5.1 ± 1.1	16
HZ 21	115	19.20	...	4.6 ± 1.0	16
Lan 23	122	20.18	...	3.2 ± 1.6	16
CPD–31 1701	131	19.39	...	3.7 ± 0.6	1

Note. — The reference numbers refer to $N(\text{H})$, $N(\text{D})$, and $N(\text{O})$, respectively. When only one reference is given it refers to all the N quoted for that particular sightline. The second part of the table contains sightlines for which only D/O is available. These ratios are displayed in Figure 17 for comparison purposes only. For these sightlines the quoted $N(\text{H})$ are estimated by using $N(\text{O})$ and $\text{O}/\text{H} = (3.43 \pm 0.15) \times 10^{-4}$ from Meyer et al. (1998).

References. — (1) Hébrard & Moos (2003), (2) Hébrard et al. (1999), (3) Dring et al. (1997), (4) Linsky et al. (1995), (5) Wood et al. (1996), (6) Wood et al. (2000), (7) Wood et al. (2002b), (8) Piskunov et al. (1997), (9) Wood et al. (2002a), (10) Hébrard et al. (2002), (11) Kruk et al. (2002), (12) Lemoine et al. (2002), (13) Vennes et al. (2000), (14) Oliveira et al. (2005), (15) Lehner et al. (2002), (16) Oliveira et al. (2003), (17) York & Rogerson (1976), (18) York & Kinahan (1979), (19) Sonneborn et al. (2002), (20) Allen et al. (1992), (21) Gry et al. (1985), (22) This work, (23) Friedman et al. (2002), (24) Ferlet et al. (1980),

(25) Meyer et al. (1998), (26) York (1983), (27) Sonneborn et al. (2000), (28) Jenkins et al. (1999), (29) Bluhm et al. (1999), (30) Williger et al. (2005), (31) Laurent et al. (1979), (32) Friedman et al. (2005), (33) Wood et al. (2004), (34) Hoopes et al. (2003), (35) Hébrard et al. (2005).

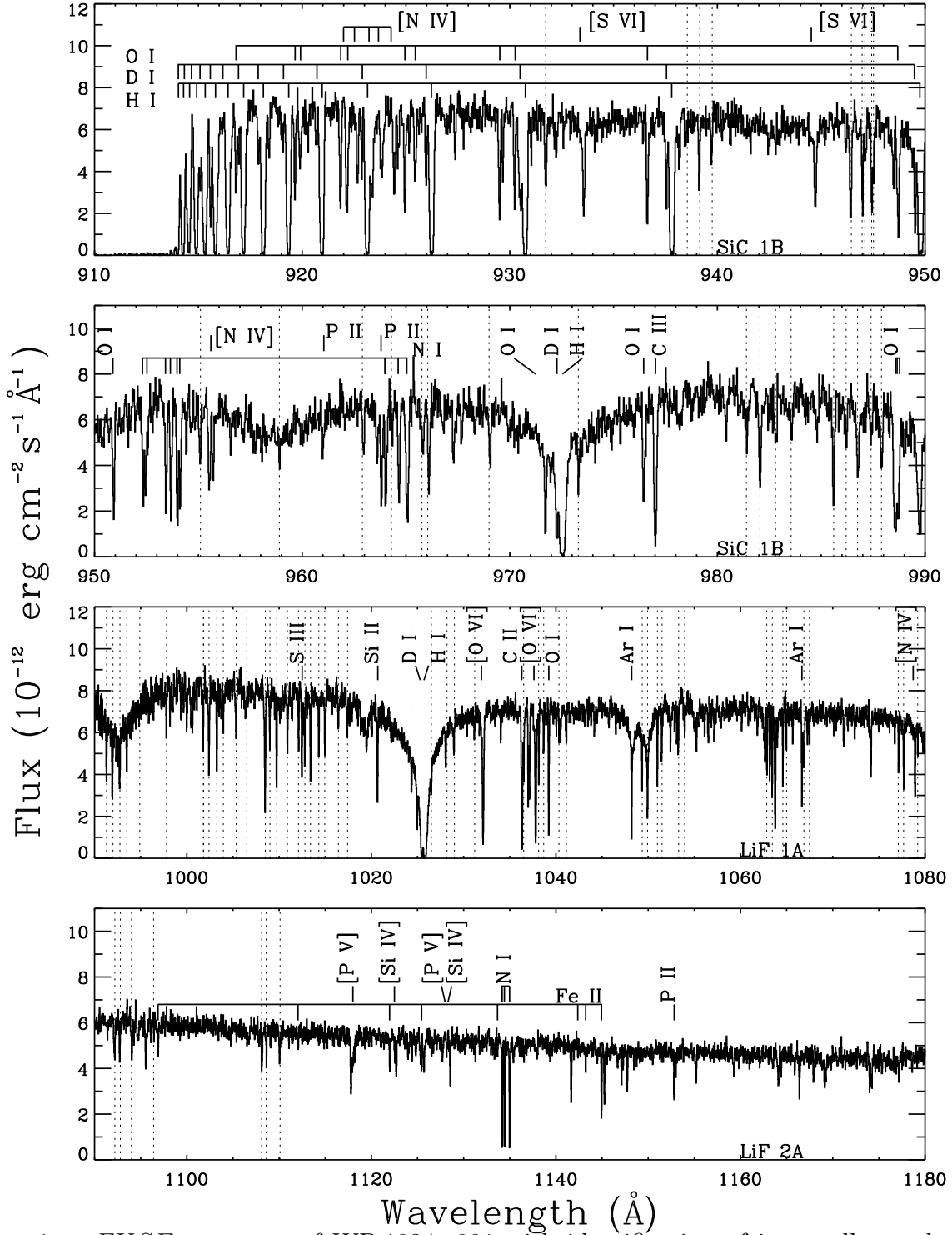


Fig. 1.— *FUSE* spectrum of WD 1034+001 with identification of interstellar and stellar absorptions. Labels in [] refer to stellar lines; dashed vertical lines mark the position of the strongest H₂ lines along this sightline. Stellar H I absorption is displaced from the ISM one by the velocity shift specified in Table 1. Note the isolated broad He II stellar lines around 992 and 958 Å. Other stellar He II lines fall close to the positions of the Ly α series and are not resolved. The *FUSE* channel used for each panel is indicated at the bottom right. The spectrum was binned by 4 for display purposes only.

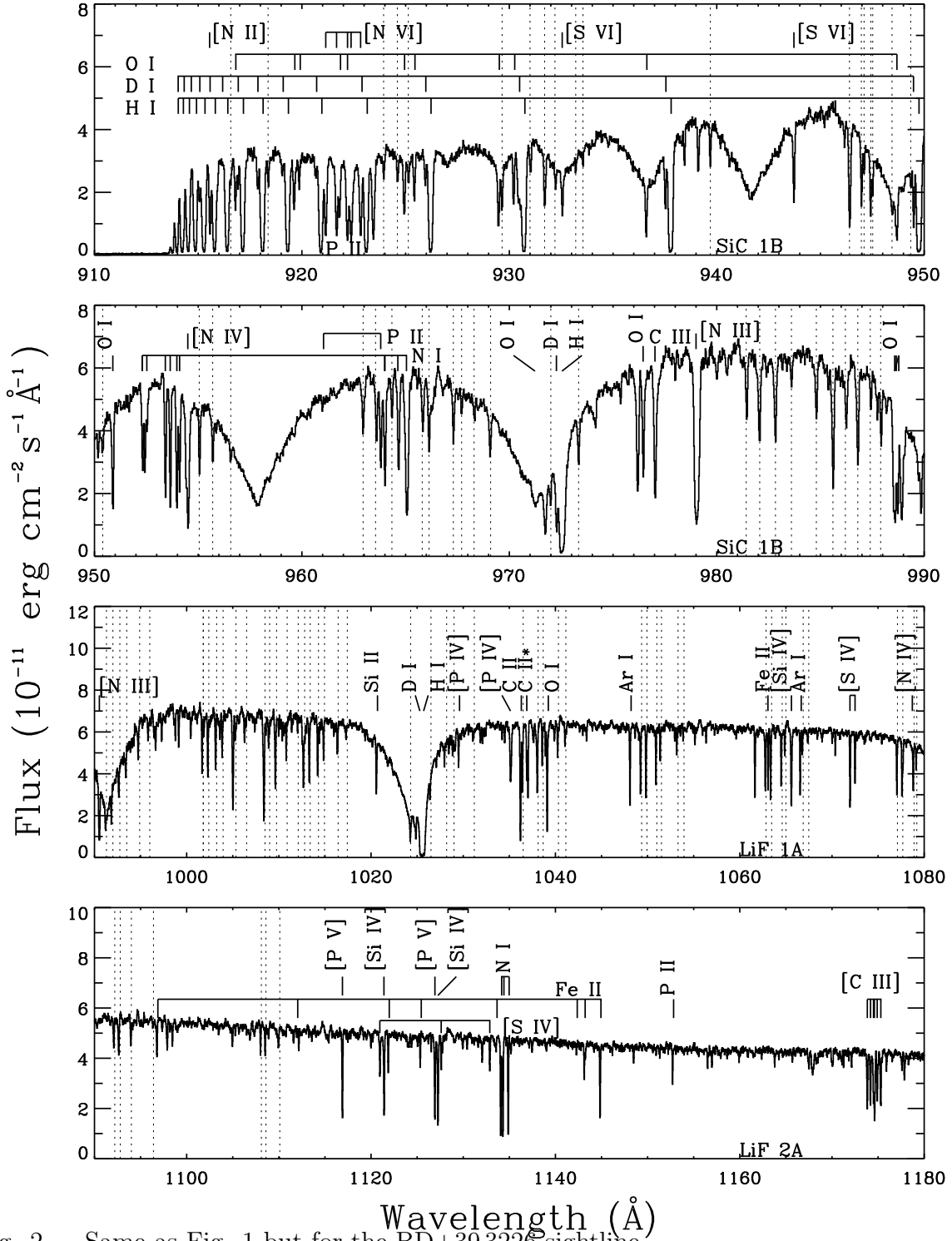


Fig. 2.— Same as Fig. 1 but for the BD+39 3226 sightline.

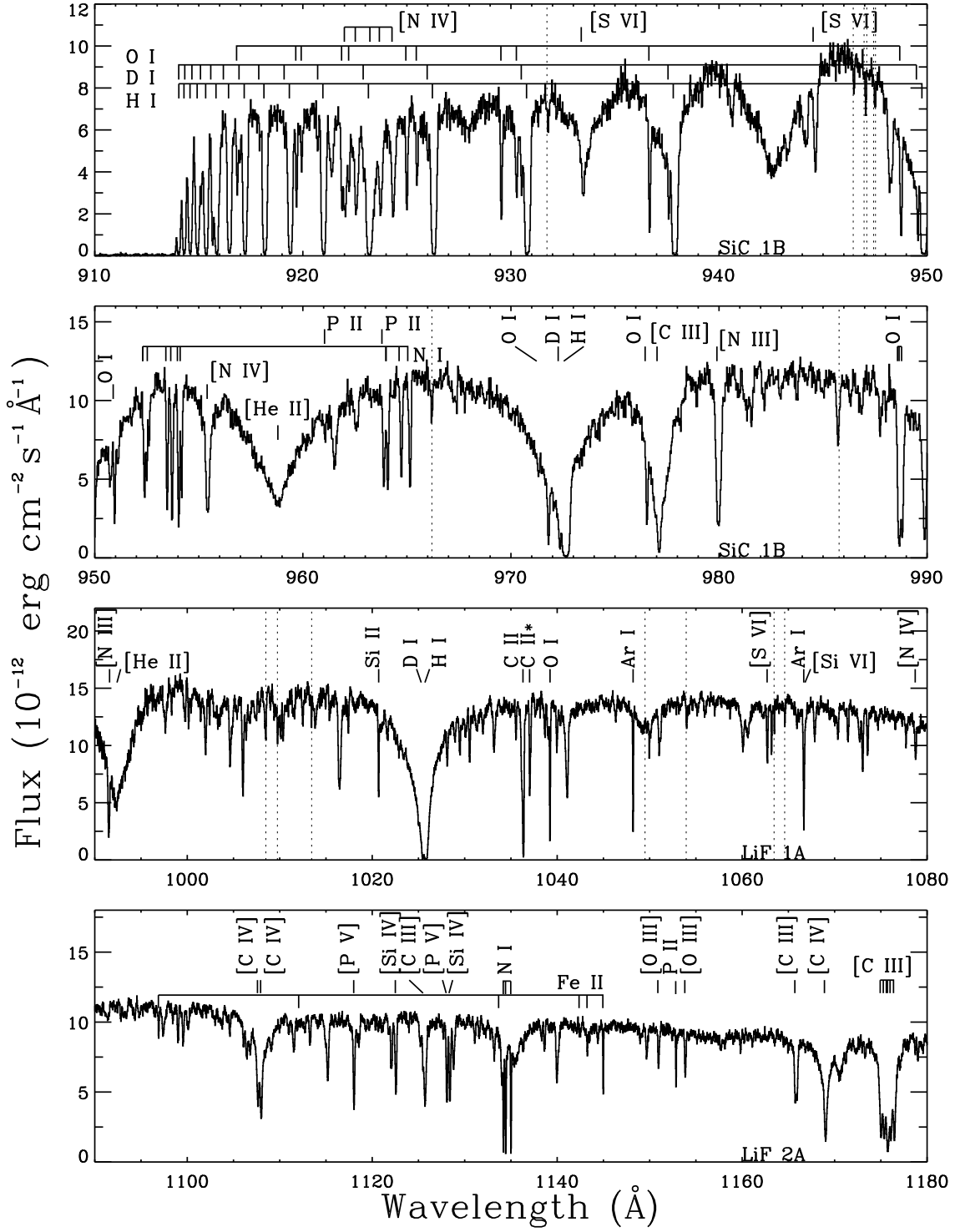


Fig. 3.— Same as Fig. 1 but for the TD1 32709 sightline.

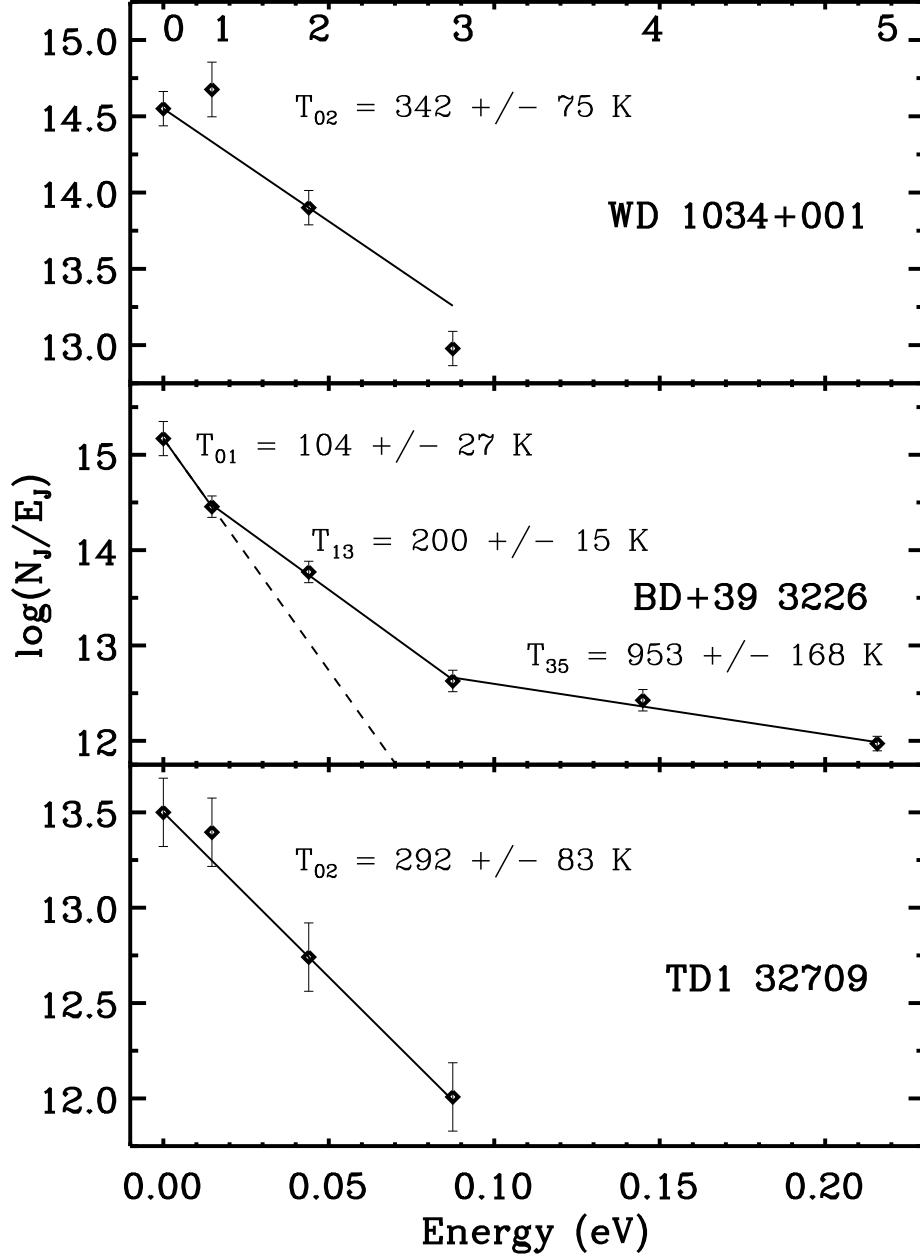


Fig. 4.— H₂ excitation diagram for the three sightlines. Each J level is labeled at the top of the first panel. See § 4.1 for discussion.

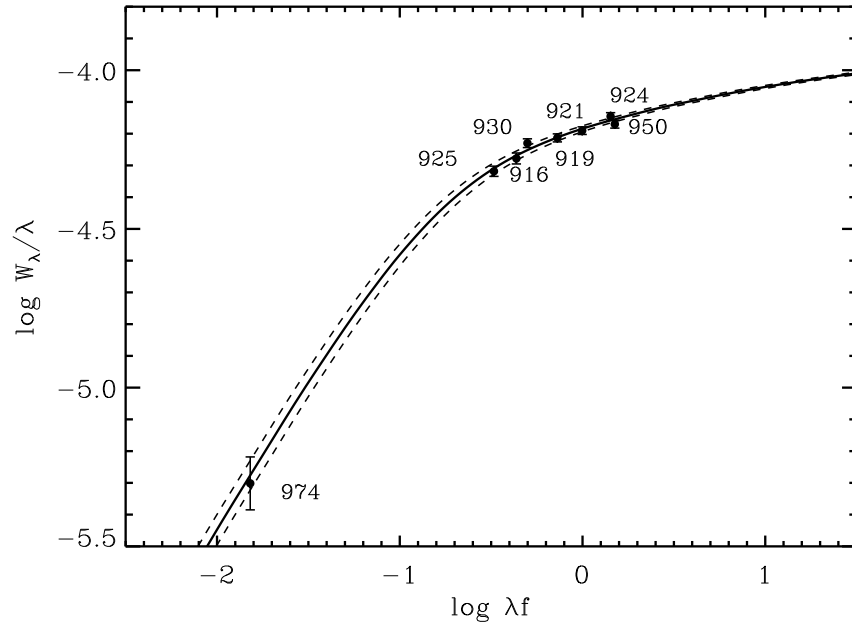


Fig. 5.— Curve of growth for O I along the WD 1034+001 sightline. We derive $\log N(\text{O I}) = 16.62 \pm 0.05$. Dashed lines indicate the 1σ uncertainty in N .

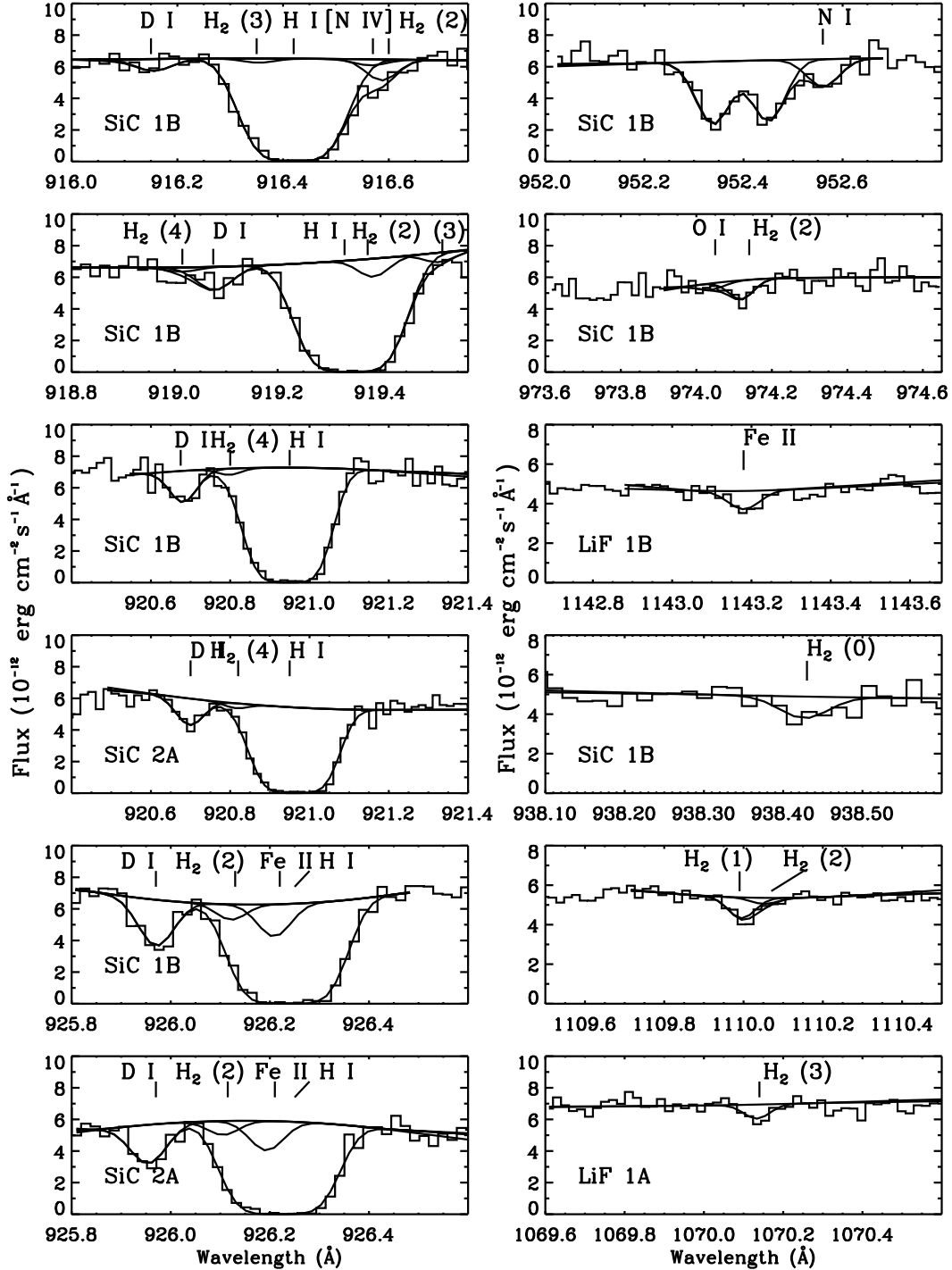


Fig. 6.— Fits to some of the lines used in the analysis of the WD 1034+001 sightline. The *FUSE* channels corresponding to the plotted data are indicated in the bottom left of each panel. For H₂, the corresponding *J* level is indicated in parenthesis. [] are used to indicate lines of photospheric origin.

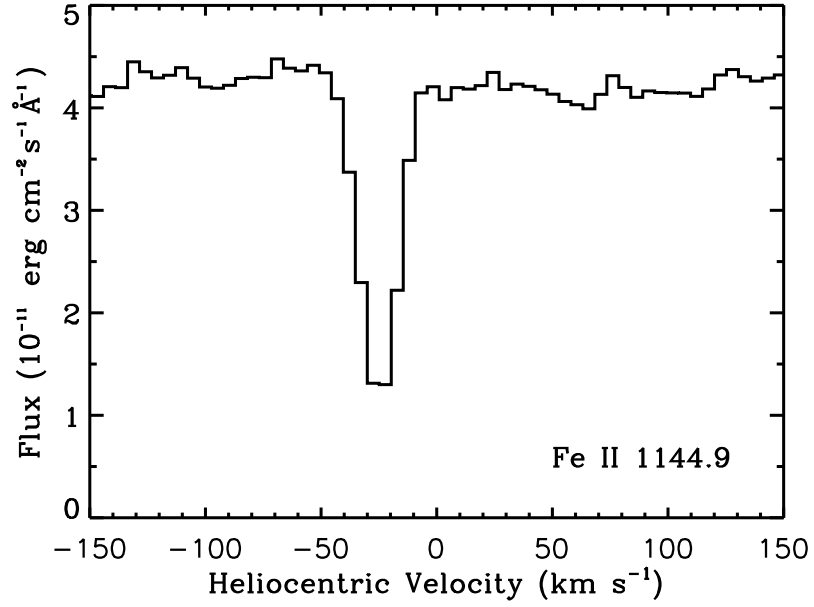


Fig. 7.— Fe II $\lambda 1144.9$ interstellar absorption toward BD+39 3226 as seen with *FUSE*. Only one absorption component, at $v_{\odot} = -25 \text{ km s}^{-1}$, is present. We see no indication of a weaker absorption component at $v_{\odot} = -75 \text{ km s}^{-1}$, as reported by Bluhm et al. (1999).

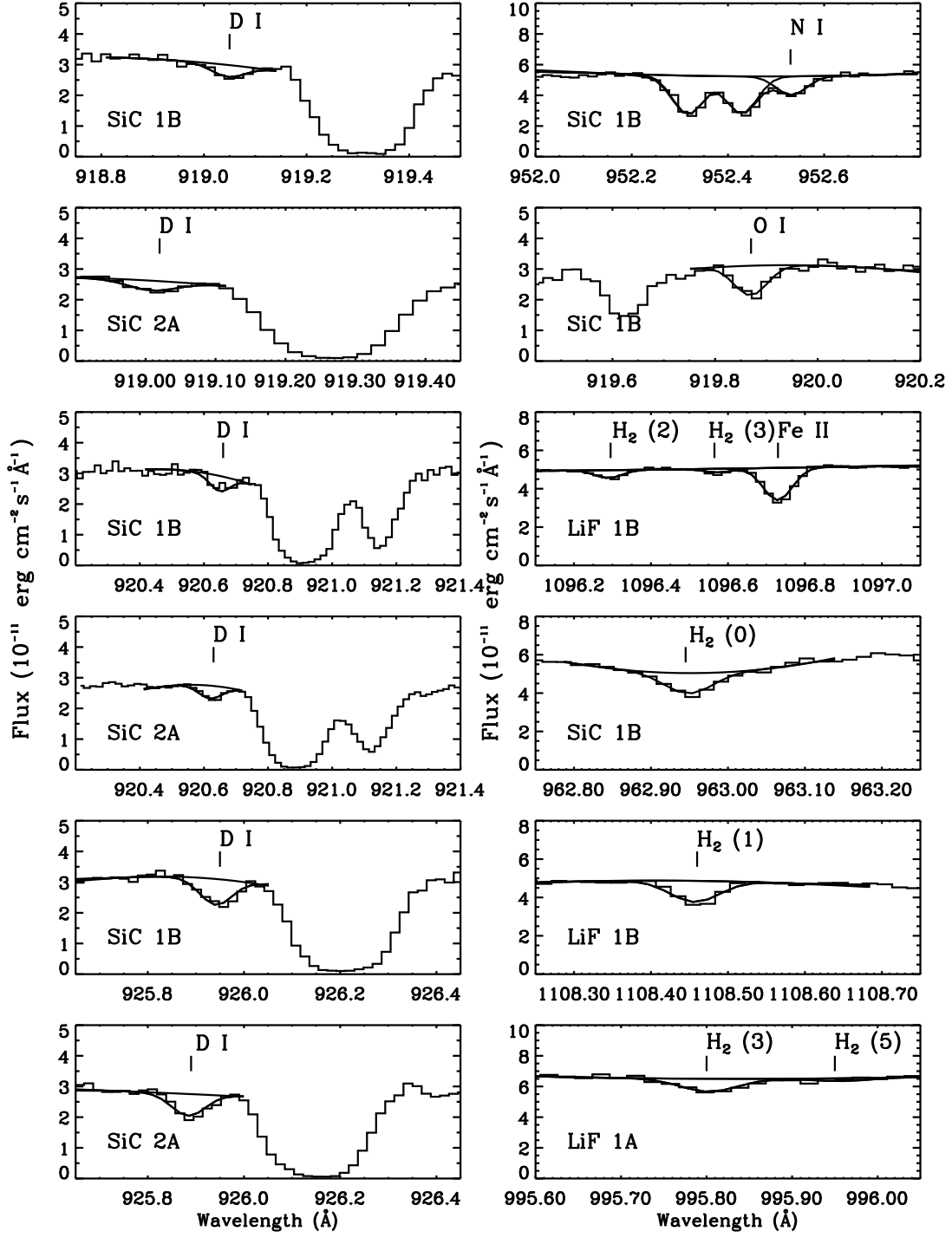


Fig. 8.— Same as Fig. 6 but for the BD+39 3226 sightline.

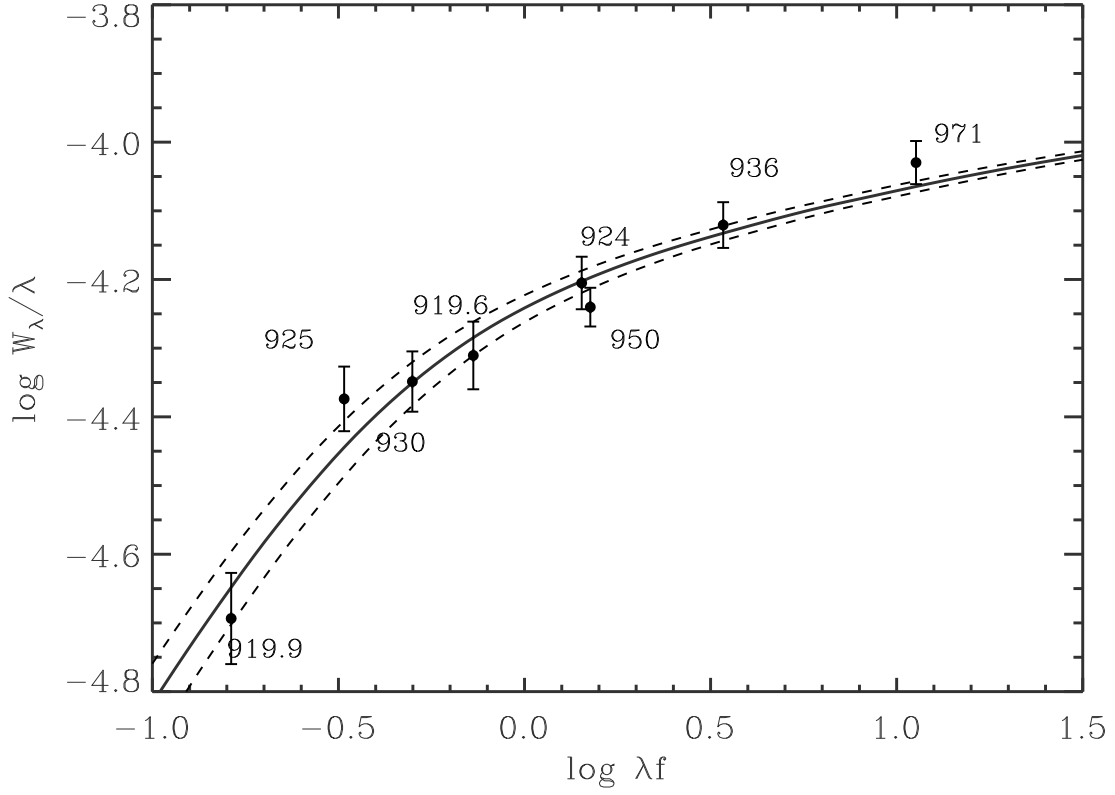


Fig. 9.— Curve-of-growth for O I along the BD+39 3226 sightline with the 1σ uncertainties in N plotted as dashed lines. The fit yields $\log N(\text{OI}) = 16.31 \pm \begin{smallmatrix} 0.07 \\ 0.06 \end{smallmatrix}$.

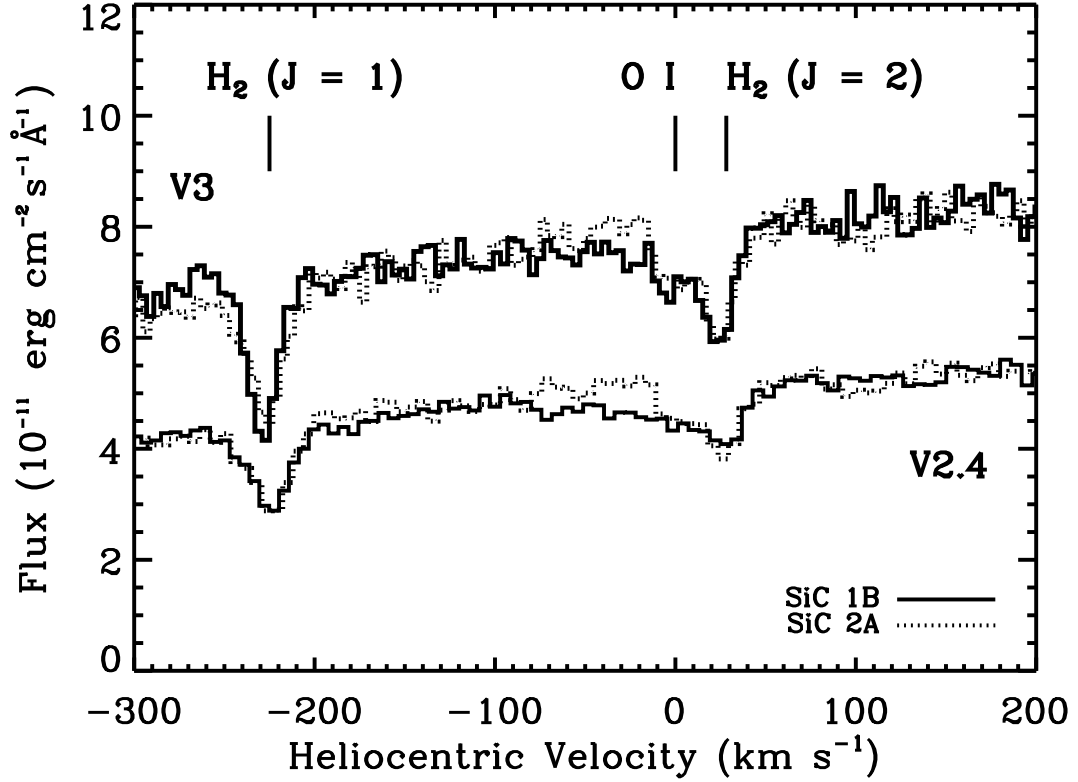


Fig. 10.— Comparison between the SiC 1B (*solid*) and SiC 2A (*dotted*) data for the BD+39 3226 sightline in the region of the O I $\lambda 974$ transition. Data at the top were calibrated with version 3 of CalFUSE (V3), data at the bottom were calibrated with version 2.4 (V2.4) (data shifted vertically for clarity). The apparent discrepancy between the profiles around O I $\lambda 974$ in the V2.4 SiC 1B and SiC 2A data disappears when V3 is used. See §4.2.2 for discussion.

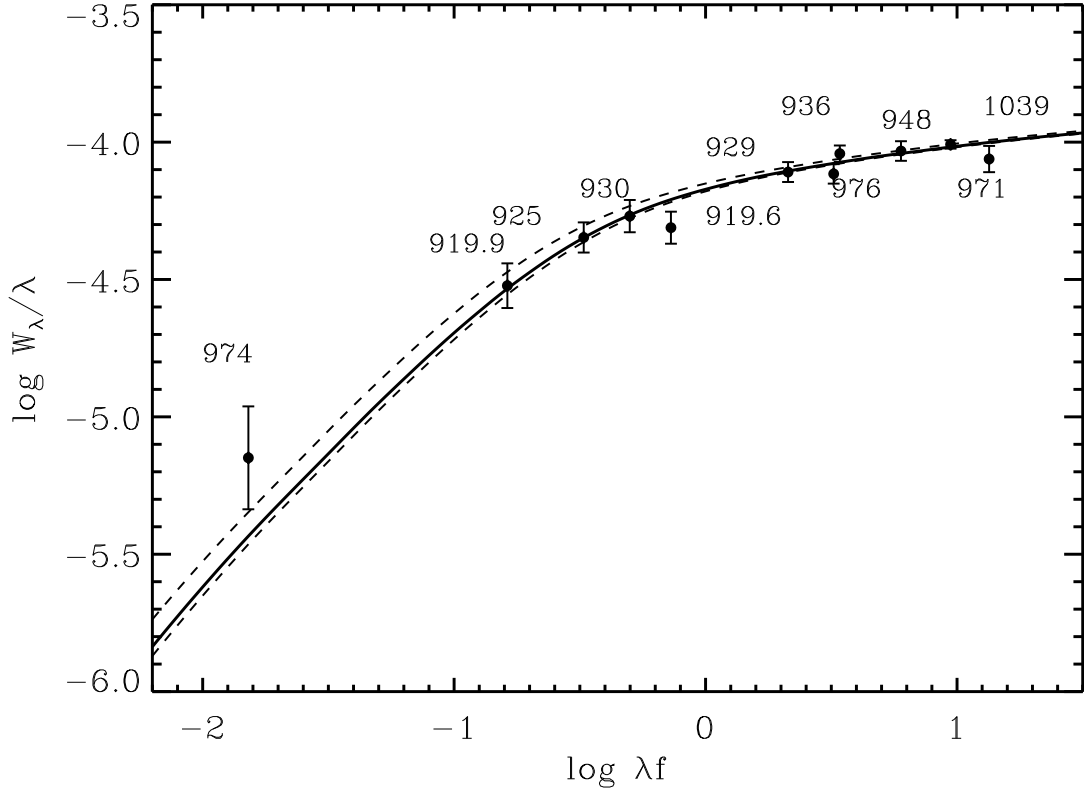


Fig. 11.— Curve of growth for OI along the TD1 32709 sightline. We derive $\log N(\text{OI}) = 16.45 \pm {}^{0.09}_{0.03}$. Dashed lines indicate the 1σ uncertainty in N .

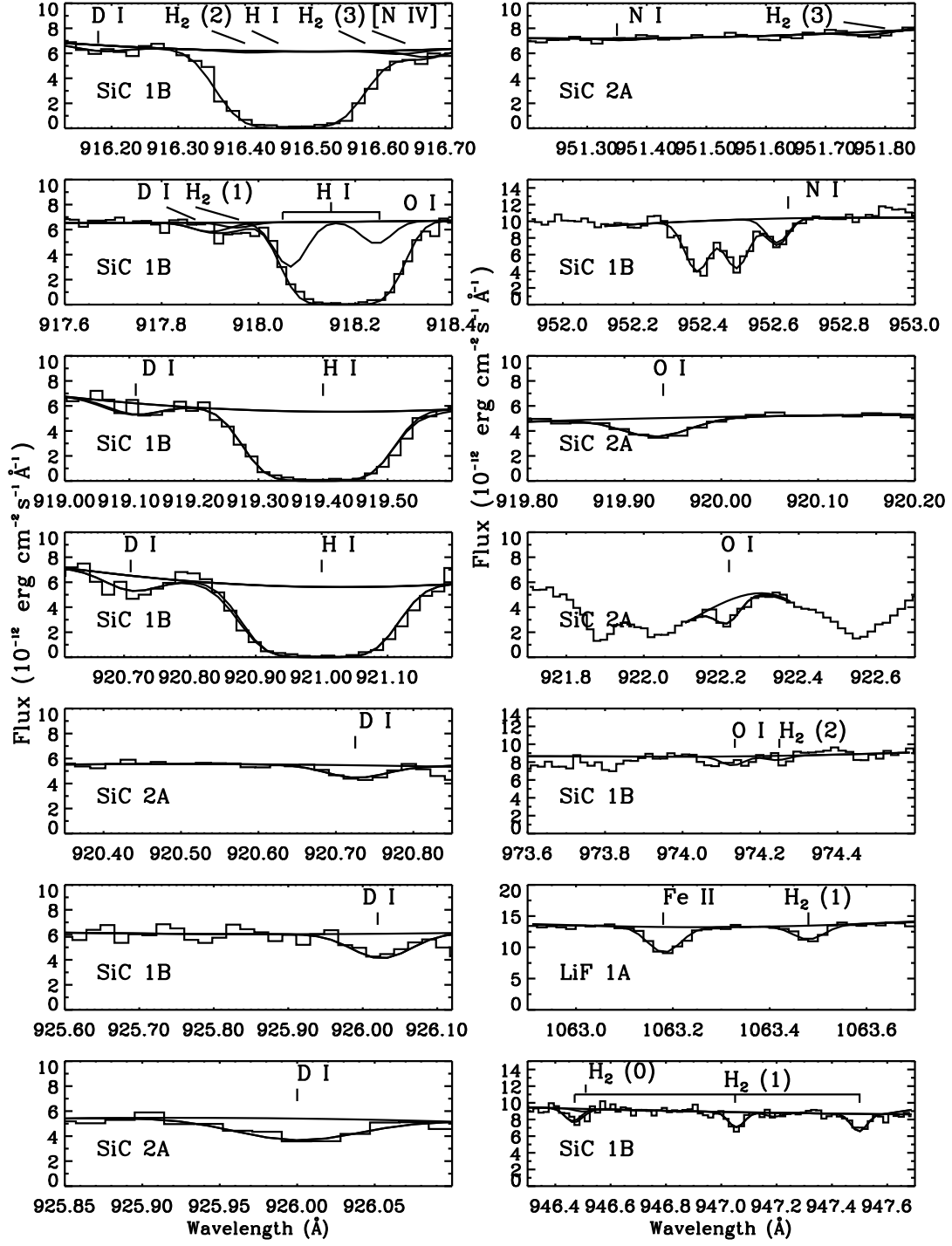


Fig. 12.— Same as Fig. 6 but for the TD132709 sightline.

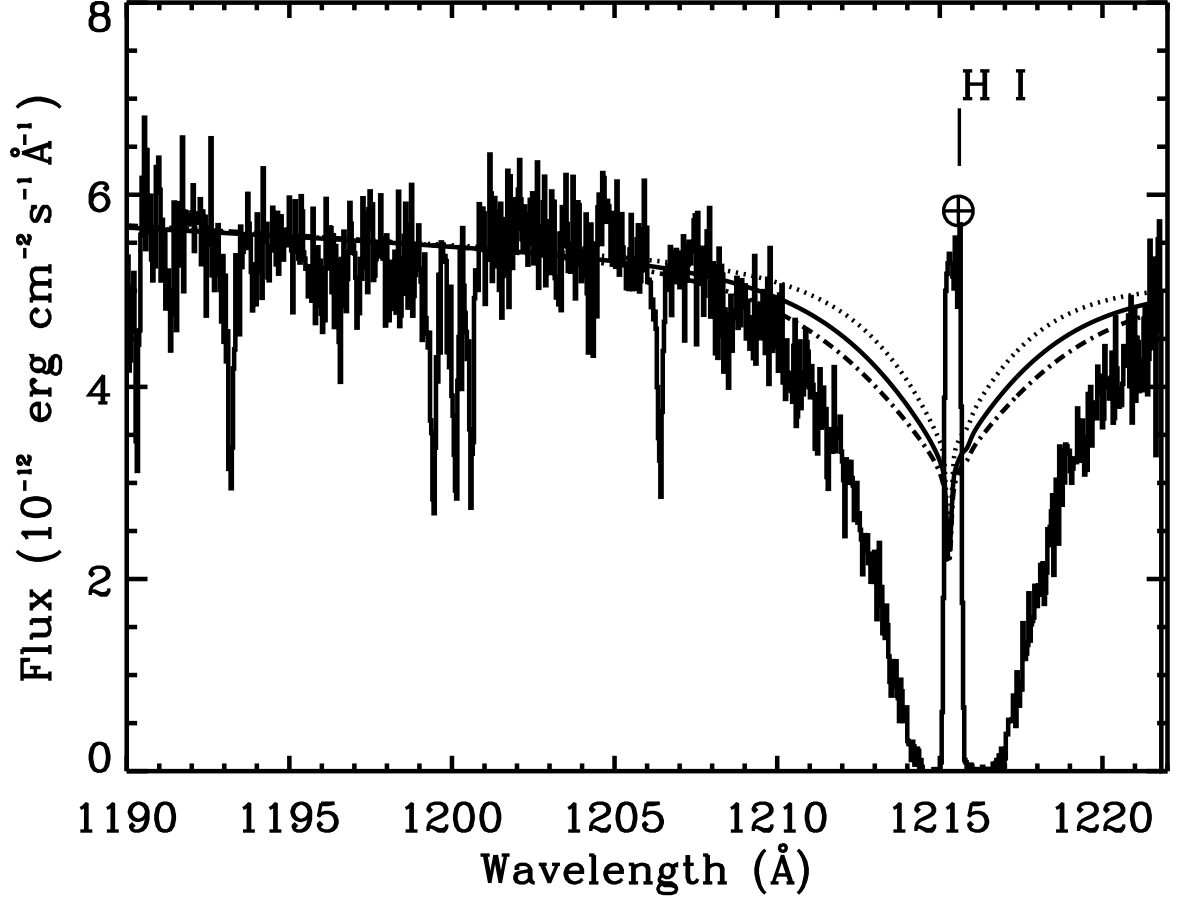


Fig. 13.— Ly α GHRs observations of the WD 1034+001 sightline. Three stellar models are overplotted: $T_{\text{eff}} = 100,000$ K, $\log g = 7.5$ (best fit model, solid line), $T_{\text{eff}} = 115,000$ K, $\log g = 7.2$ (dotted line), and $T_{\text{eff}} = 90,000$ K, $\log g = 7.8$ (dash-dotted line). All the models have $\log (\text{He}/\text{H}) = 3.0$. The two last models produce the highest and lowest $N(\text{HI})$, respectively, and are used to determine the uncertainties in $N(\text{HI})$ associated with the stellar models. Geocoronal emission is annotated with \oplus . We derive $\log N(\text{HI}) = 20.07 \pm 0.07$ (1σ).

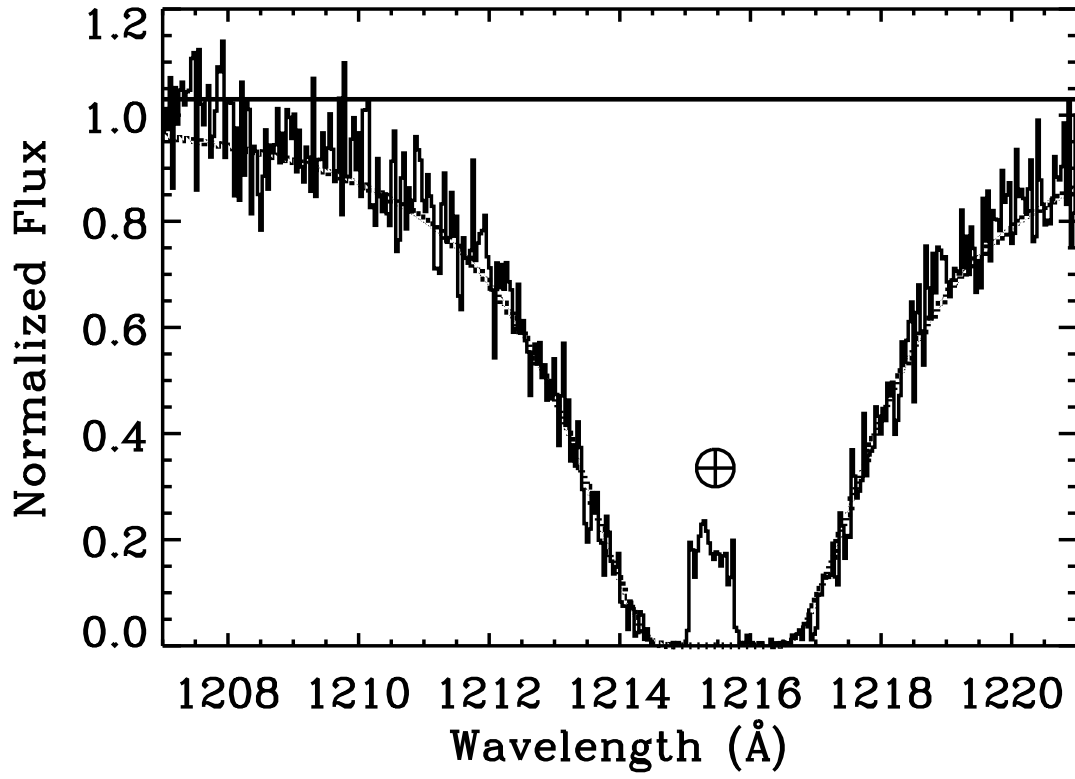


Fig. 14.— Fit to the Ly α interstellar absorption along the WD 1034+001 sightline, using the best fit stellar model to normalize the data. Terrestrial airglow is labeled with \oplus .

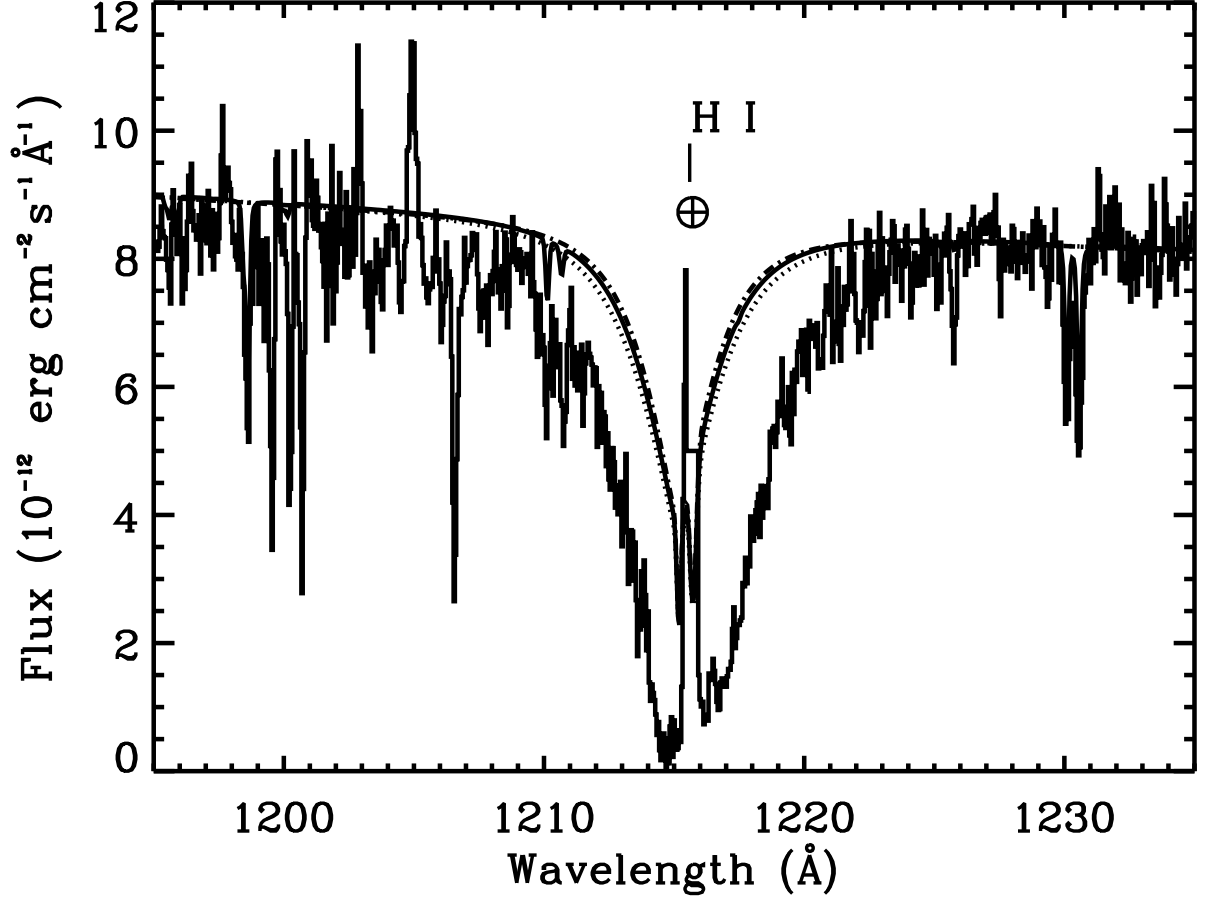


Fig. 15.— Ly α *IUE* observations of the TD132709 sightline. Three stellar models are overplotted: $T_{\text{eff}} = 46,500$ K, $\log g = 5.55$ (best fit model, solid line), $T_{\text{eff}} = 45,000$ K, $\log g = 5.7$ (dotted line), and $T_{\text{eff}} = 47,500$ K, $\log g = 5.4$ (dash-dotted line). All the models have $\log(\text{He}/\text{H}) = 2.0$. The two last models produce the lowest and highest $N(\text{HI})$, respectively, and are used to determine the uncertainties in $N(\text{HI})$ associated with the stellar models. Geocoronal emission is annotated with \oplus . We derive $\log N(\text{HI}) = 20.03 \pm 0.10$ (1σ).

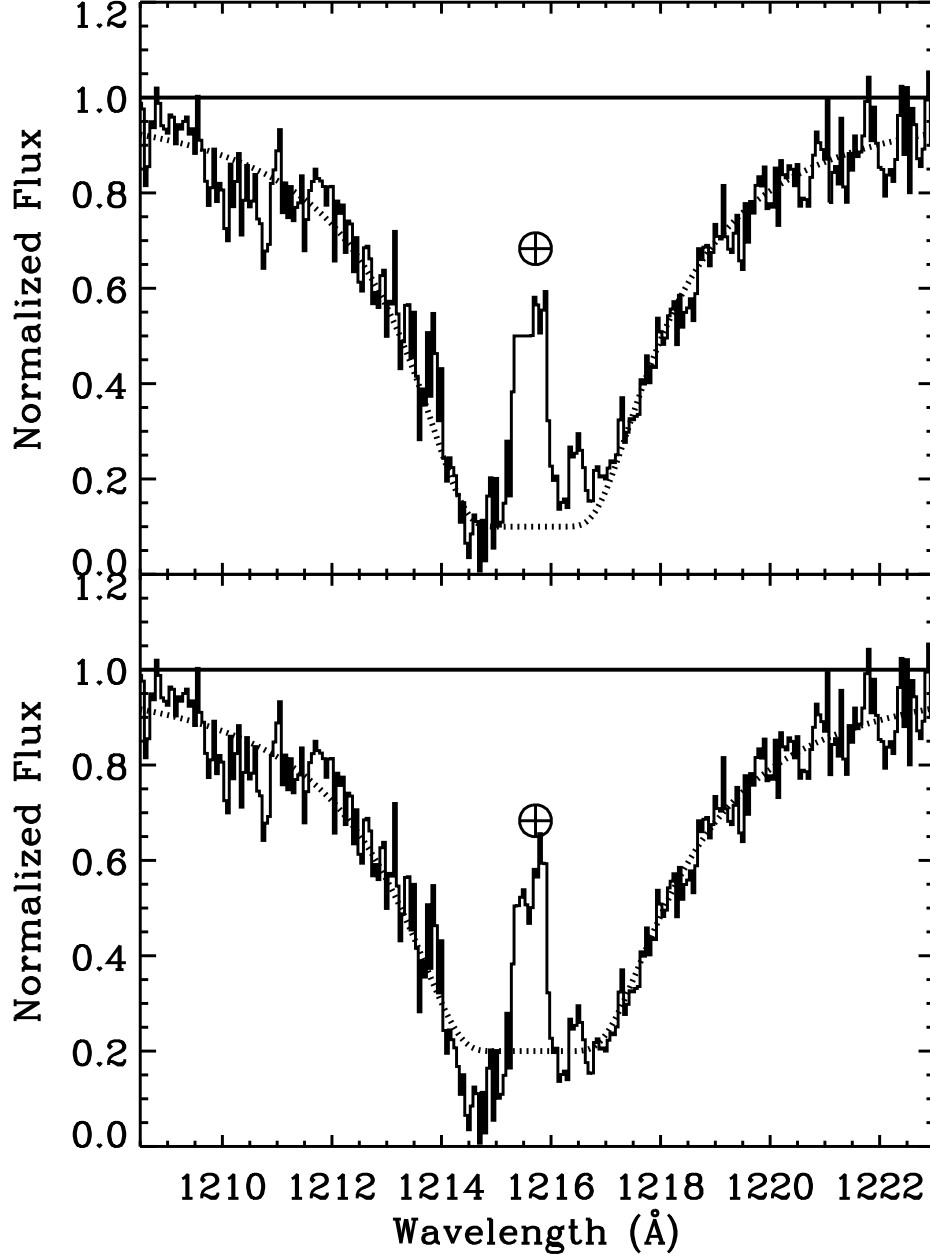


Fig. 16.— Fit to the Ly α interstellar absorption along the TD1 32709 sightline, using the best fit stellar model to normalize the data. *Top panel:* The blue wing of the Ly α line is used to define the zero flux level, yielding $\log N(\text{HI}) = 20.03$. *Bottom panel:* The red wing of the Ly α line is used to define the zero flux level, yielding $\log N(\text{HI}) = 20.12$, within the 1σ uncertainty quoted in Table 9 for $N(\text{HI})$ along this sightline.

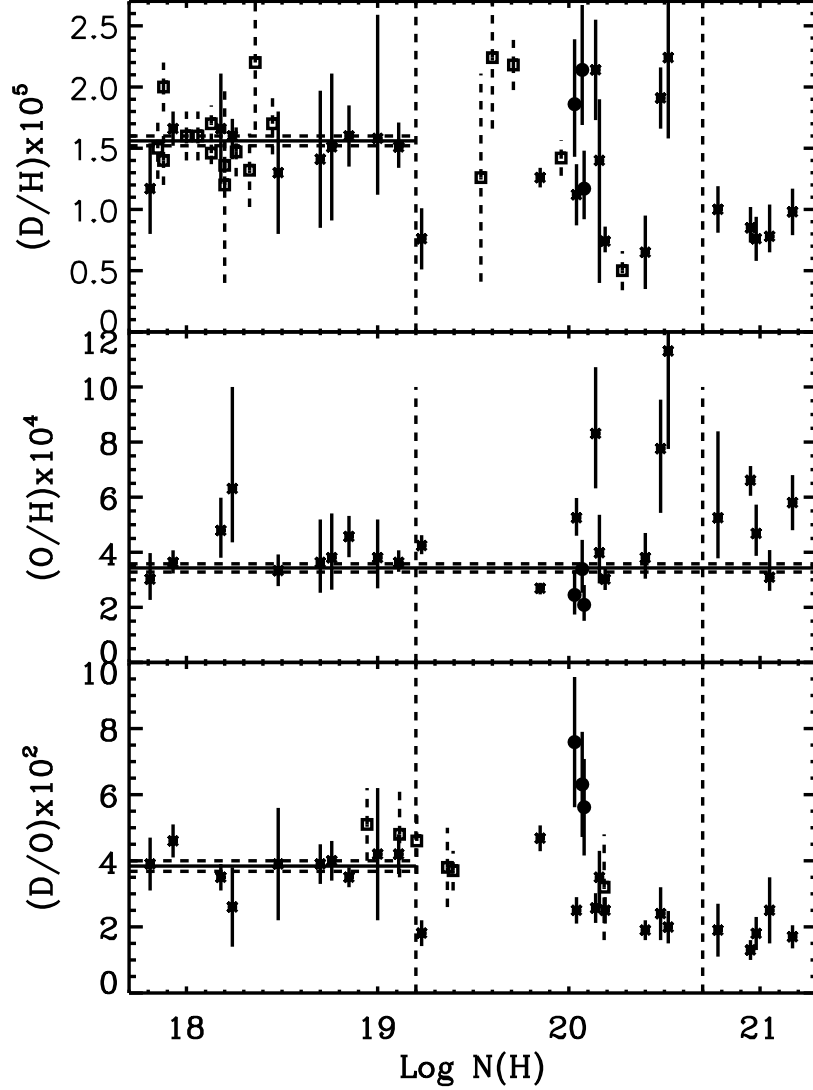


Fig. 17.— D/H, O/H, and D/O ratios as a function of the sightline total hydrogen column density, $N(\text{H})$. Sightlines for which all three D/H, O/H, and D/O ratios are available are marked by asterisks (literature values) and filled circles (this work). *Top panel:* Sightlines for which no OI measurement is available are marked with squares, the error bars are displayed by dotted lines. $(\text{D}/\text{H})_{\text{LB}} = (1.56 \pm 0.04) \times 10^{-5}$ (derived by Wood et al. 2004, from a compilation of values in the literature) is indicated by solid and dashed (1σ) horizontal lines for $\log N(\text{H}) < 19.2$, which defines the contour of the Local Bubble (dashed vertical line). For $19.2 < \log N(\text{H}) < 20.7$ there is a large scatter in the D/H ratio. For $\log N(\text{H}) > 20.7$, D/H seems to be constant, but lower than the LB value. *Middle panel:* The $\text{O}/\text{H} = (3.43 \pm 0.15) \times 10^{-4}$ derived by Meyer et al. (1998) is marked by solid and dashed (1σ) horizontal lines. *Bottom panel:* $\text{D}/\text{O} = (3.84 \pm 0.16) \times 10^{-2}$ derived by Hébrard & Moos (2003) for the LB is marked by solid and dashed (1σ) horizontal lines. Sightlines for which no $N(\text{H})$ is available are indicated by squares, the uncertainties are displayed by dotted lines. For these sightlines we use $N(\text{OI})$ and the O/H ratio derived by Meyer et al. (1998) to estimate $N(\text{H})$.

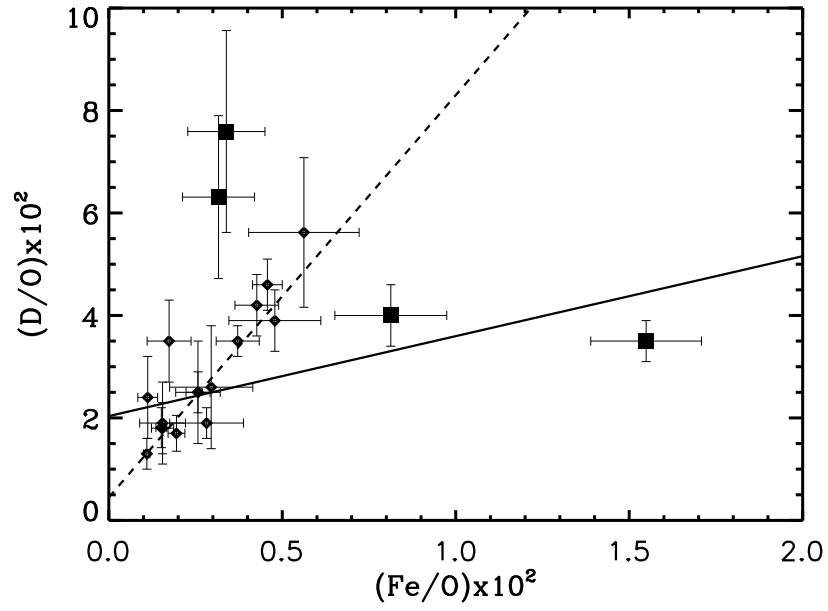


Fig. 18.— D/O as a function of Fe/O . The solid line represents the fit to all the data points presented. The dashed line represents the fit to the data when the four data points displayed by squares are removed from the fit. See §7.2 for discussion.

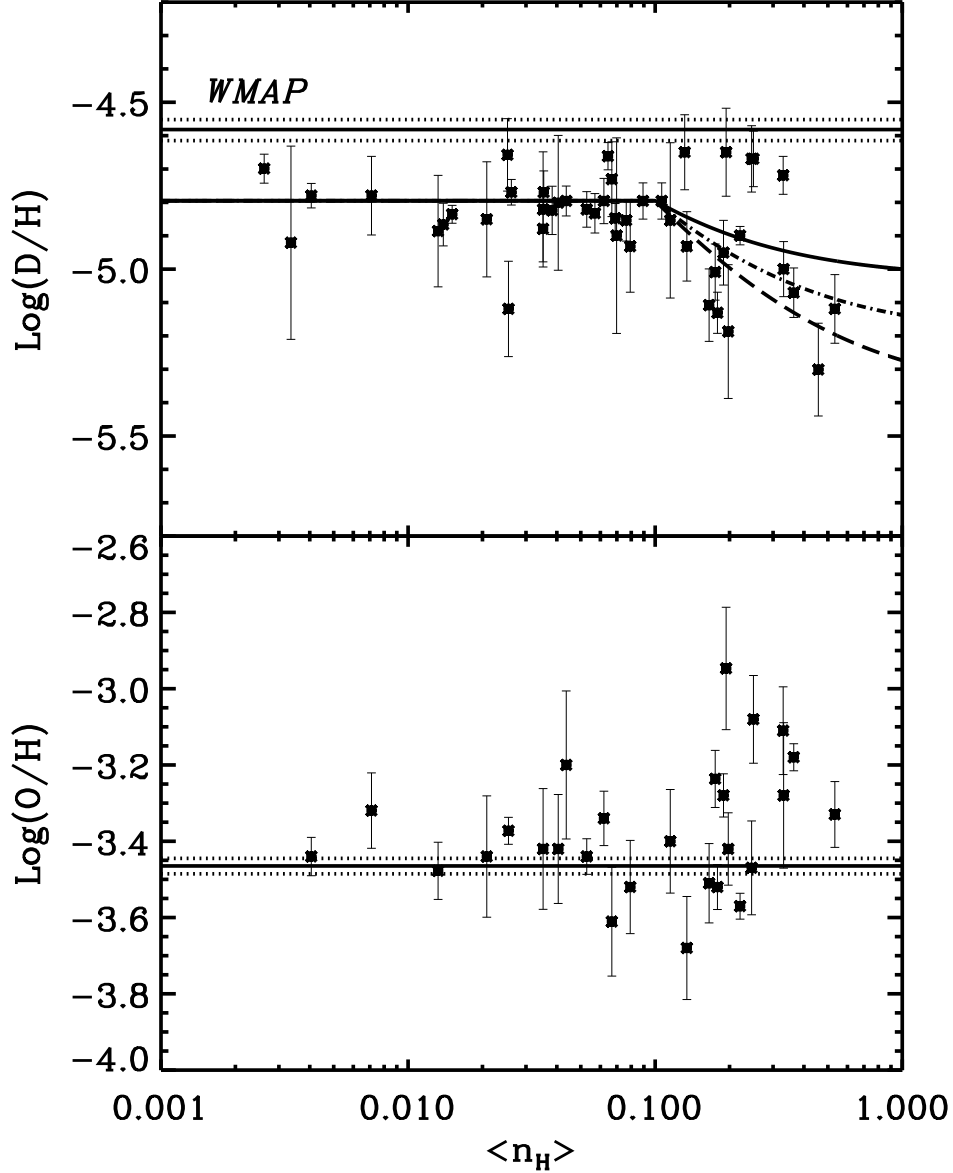


Fig. 19.— *Top panel:* $\text{Log}(D/H)$ as a function of the average sightline density, $\langle n_H \rangle$ (cm^{-3}). The *WMAP*-based result of $(D/H)_{\text{prim}} = (2.62 \pm_{0.20}^{0.18}) \times 10^{-5}$ (Spergel et al. 2003) is also plotted (*solid* and *dotted* lines at $\text{log}(D/H) = -4.57$). The *solid* line represents the fit of Equation 2 to all data points, yielding $A_w(D) = -4.80$ ($D/H = 1.58 \times 10^{-5}$) and $A_c(D) = -5.03$ ($D/H = 0.93 \times 10^{-5}$). The *dash-dotted* and *dashed* lines correspond to $A_c(D) = -5.20$ ($D/H = 0.63 \times 10^{-5}$) and $A_c(D) = -5.38$ ($D/H = 0.42 \times 10^{-5}$), respectively. See §7.3 for discussion. *Bottom panel:* $\text{Log}(O/H)$ as a function of $\langle n_H \rangle$. The *solid* and *dashed* lines represent $O/H = (3.43 \pm 0.15) \times 10^{-4}$ derived by Meyer et al. (1998).